NASA CONTRACTOR REPORT

NASA CR-2262

NASA CR-2262

BUMPER-PROTECTED LAMINATED SPACECRAFT MAINWALLS

by Ray Kinslow

Prepared by
TENNESSEE TECHNOLOGICAL UNIVERSITY
Cookeville, Tenn. 38501
for Langley Research Center

NATIONAL AERONAUTICS AND SPACE ADMINISTRATION • WASHINGTON, D. C. • MAY 1971

1. Report No.	2. Government Accession No.	3. Recipient's Catalog No.
NASA CR-2262		

4. Title and Subtitle	5. Report Date
BUMPER-PROTECTED LAMINATED SPACECRAFT MAINWALLS	May 1973
	6. Performing Organization Code

7. Author(s)	8. Performing Organization Report No.
Ray Kinslow	
	10. Work Unit No.

9. Performing Organization Name and Address	11. Contract or Grant No.
Department of Engineering Science Tennessee Technological University Cookeville, Tennessee 38501	NAS 1-10967
	13. Type of Report and Period Covered
12. Sponsoring Agency Name and Address National Aeronautics and Space Administration Washington, D.C. 20546	Contractor Report
	14. Sponsoring Agency Code

15. Supplementary Notes

16. Abstract

A study is made of the meteoroid impact resistance of bumper-protected mainwalls of both solid aluminum and polycarbonate-aluminum laminates. Semi-empirical models of the debris cloud and stress waves are formulated. Results indicate that a laminated mainwall affords greater impact resistance than a solid aluminum mainwall of the same weight.

17. Key Words (Suggested by Author(s))		18. Distribution Statement
Hypervelocity Impact	Spallation	Unclassified – Unlimited
Meteor Bumper	Failure	
Laminated Structures		
Stress Waves		
Spacecraft		

19. Security Classif. (of this report)	20. Security Classif. (of this page)	21. No. of Pages	22. Price*
Unclassified	Unclassified	62	$3.00

*For sale by the National Technical Information Service, Springfield, Virginia 22151

CONTENTS

NOMENCLATURE

A	Debris distribution factor
B, n	Spray dispersion factors
c_1	Longitudinal wave velocity
c_2	Shear wave velocity
E	Young's modulus
F	Forcing function
K	A constant
m	Projectile mass
M	Momentum multiplication factor
O'	Apparent origin of debris cloud
O_1	Center of cavity in which incident wave is assumed to originate
O_2	Center of cavity in which reflected wave is assumed to originate
p	Pressure per unit area
P	A point
r	Radius vector
R_o	Radius of an imaginary cavity
R_1	Distance from O_1 to point P
R_2	Distance from O_2 to point P
RL	Reflected longitudinal wave
RS	Reflected shear wave
t	Time
T_1	Thickness of first laminate
T_2	Thickness of second laminate

TL	Transmitted longitudinal wave
TS	Transmitted shear wave
TRL	Longitudinal wave after transmission and reflection
TRS	Shear wave after transmission and reflection
u	Particle displacement
v	Projectile and debris velocities
x, y	Coordinates
Y	Sum of bumper spacing, bumper thickness, and projectile diameter
α_1, α_2	Decay constants
τ, μ	Lamé constants
ν	Poisson's ratio
θ, ϕ, β	Angles (see Figures 1, 8, and 16)
ϕ	A scalar displacement potential
ρ	Material density
σ_r	Radial stress
σ_θ	Tangential stress
τ, α_o, ω_o	Defined on page 5
γ	Direction of maximum principal stress

BUMPER-PROTECTED LAMINATED SPACECRAFT MAINWALLS

By Ray Kinslow
Department of Engineering Science
Tennessee Technological University

1. INTRODUCTION

It was first suggested by Whipple (Reference 1) that a thin shield spaced some distance from the mainwall of a spacecraft would completely fragment a meteoroid and disperse the resulting debris over a large area of the main structure inflicting only slight damage. Many subsequent investigators have confirmed the fact that such a shield or bumper can significantly reduce meteoroid impact damage to the structure.

It has also been demonstrated that laminated mainwalls can be utilized to reduce the damage resulting from hypervelocity impact (Reference 2).

This study is an investigation of the effects of employing the use of both a bumper and a laminated spacecraft mainwall to reduce the meteoroid hazard to space vehicles. A quasi-theoretical approach has been taken. A mathematical model has been formulated that gives results that are in good agreement with experimental data.

2. DEBRIS CLOUD PRODUCED BY PROJECTILE-BUMPER INTERACTION

As previously stated, the bumper serves to fracture the hypervelocity projectile and to diverge its fragments. Various assumptions and computations as to the debris cloud characteristics have been made by many different investigators.

It is assumed that the origin of the debris cloud is one projectile diameter in front of the bumper. This is the conclusion reached by several investigators. Turpin (Reference 3, p. 118) says, "This location appears to vary slightly with material, but generally corresponds to the rear surface of the projectile at the first instant of impact." According to Rosenblatt (Reference 4, p. 69), "The velocity distribution in the debris cloud indicates that the mass elements making up that cloud have the appearance of emanating from just ahead of the target surface. The average intercept of the velocity vectors with the axis is about one projectile diameter ahead of the target for all impact cases considered." This assumed point of origin of the debris is indicated by point O' in Figure 1. Its distance from the main structure is Y, the sum of bumper spacing, bumper thickness, and projectile diameter.

In order to treat the problem theoretically, Maiden, et al (Reference 5, p. 21) assumed that the fragments loaded the mainwall uniformly over a circular area of diameter equal to one-half the bumper spacing. This is indicated by the rectangle in Figure 2 which shows the normalized axial component of momentum of the debris per unit area. In a later study of the ballistic limit of

double-walled meteoroid systems, Madden (Reference 6, p. 9) assumed that the mass distribution of the spray particles could be approximated by a normal Gaussian distribution. Assuming that the momentum applied to the mainwall has the same distribution as that of the mass discussed by Madden, it can be described by the relation, mom = $e^{-9\tan^2\theta}$. This is also shown in Figure 2.

In an analytical study of debris clouds due to impacts on thin plates, Rosenblatt, et al utilized the STEEP code to obtain numerical solutions (Reference 4). The axial momentum per unit area produced by the impact of a 1/8-inch aluminum sphere on a 1/32-inch aluminum plate at a velocity of 24,600 ft/sec is shown in Figure 2. This is in close agreement with the Gaussian distribution, especially for larger angles of dispersion.

It was pointed out in Reference 4, page 35, that three regions of the momentum (as well as mass and energy) distribution curves can generally be recognized. The first region is due to the main body of the debris cloud and the most severe damage to the mainwall will be caused by the impact of these fragments. This region is confined to an included half-angle of less than 20 degrees.

The momentum distribution per unit area used in this study is assumed to be proportional to $(1 - A \tan^2\theta)$, where θ is the included half-angle and A is a debris distribution factor. This is shown in Figure 1 with A having a value of 6. This is in good agreement with the values computed for the Al-Al impact for angles up to about 17 degrees which includes the area where damage is most likely to occur.

This more simple expression was used because: (1) For the material combination being considered for the laminated mainwall, there is a total reflection of the longitudinal waves at an angle of about 25 degrees; (2) It has been pointed out that damage will probably be limited to an included half-angle of less than 20 degrees; and (3) Mathematical and computer difficulties were encountered in assuming a Gaussian distribution.

It is assumed that the leading edge of the debris cloud travels at the projectile impact velocity. According to Reference 4, page 58, the ratio of cloud velocity to projectile velocity varies from 0.92 to 1.0 for Al-Al impact at velocities of 0.75 and 1.5 cm/μsec, respectively. This ratio is slightly greater than unity for copper and cadmium impacts. Swift and Prater (Reference 7, p. 11) give a cloud-to-projectile velocity ratio of about 0.95 on the cone axis to 0.85 at an angle of 20 degrees for Cd-Cd impact at 0.67 cm/μsec. This assumption appears to be reasonable in view of both experimental and theoretical results.

Many excellent photographs have been made of debris clouds. Figure 3, taken from page 3 of Reference 8 is one such photograph. As the envelope of the debris resembles a Lemniscate of Bernoulli, it was suggested that this curve might be used as a mathematical model of the cloud. True Lemniscates are shown in Figure 4. Although these resemble the cloud photographs, the

angle of 90 degrees formed by the tangents at point 0 is too large. Several modifications are shown in Figure 5. The curve, $r^2 = \cos 3\theta$, most accurately matches the cloud photograph. Figure 6 shows the cloud profiles at various times based upon this model.

If the projectile and debris velocity is denoted by v and time is measured from the instant of the first mainwall impact, the time at which any portion of the cloud at a cone angle of θ reaches the wall is given by the relation

$$t = \frac{Y}{v}\left[\frac{1}{\cos\theta(\cos B\theta)^n} - 1\right] \qquad (1)$$

where B and n are spray dispersion factors, having values of 3 and 1/2, respectively, in this example.

3. MAINWALL LOADING

The loading of the spacecraft's hull by the fragments in the debris cloud is a function of many factors including the mass and velocity of the projectile, the bumper spacing, the debris distribution, the cloud dispersion, and the momentum multiplication.

The characteristics of the debris cloud have been discussed. The momentum multiplication factor results from two multiplication effects. The first results from the projectile impact on the bumper and the second results from the reflection of gas and debris from the hull. Cunningham (Reference 8, p.47), Maiden (Reference 5, p. 21), and many other investigators agree that for most metals the momentum transferred to the mainwall is equal to approximately twice the momentum of the original projectile.

Because the debris cloud is practically hollow and its wall thickness is small (Reference 4, p. 57), and also because the fragments are very small, it is obvious that the loading time at any point is extremely short (Reference 5, p. 21).

It is assumed that the mainwall pressure per unit area can be specified by the relation

$$p \approx e^{-\alpha_1 t} - e^{-\alpha_2 t} \qquad (2)$$

where α_1 and α_2 are decay constants and t is time. For any desired rise and decay times, the values of the decay constants can be determined from the chart of Figure 7.

The normal pressure (see Figure 1) on the mainwall surface is

$$p = K(1-A\tan^2\theta)(e^{-\alpha_1 t} - e^{-\alpha_2 t}) \qquad (3)$$

$$p_y = K \cos\theta(1-A \tan^2\theta)(e^{-\alpha_1 t} - e^{-\alpha_2 t}) \tag{4}$$

where K is a constant depending upon several parameters.

Equating the product of the projectile momentum and the momentum multiplication factor to the total normal component of the momentum applied to the mainwall gives the relation

$$M(mv) = \int_{t=0}^{\infty} \int_{\theta=0}^{\tan^{-1}A^{-0.5}} p_y \, da \, dt \tag{5}$$

where

$$da = 2\pi r_x dr_x = 2\pi Y^2 \sec^2\theta \tan\theta \, d\theta \tag{6}$$

therefore

$$M(mv) = 2\pi KY^2 \iint (1-A \tan^2\theta)(e^{-\alpha_1 t} - e^{-\alpha_2 t}) \sec\theta \tan\theta \, d\theta \, dt \tag{7}$$

$$= 2\pi KY^2 \left[\frac{\alpha_2-\alpha_1}{\alpha_1\alpha_2}\right]\left[\frac{2(A+1)^{1.5}}{3A^{0.5}} \; \frac{3+2A}{3}\right] \tag{8}$$

If the debris distribution factor is 6 (max θ = 22.2°)

$$M(mv) = 0.307 \; KY^2 \left[\frac{\alpha_2-\alpha_1}{\alpha_1\alpha_2}\right] \tag{9}$$

4. PROPAGATION OF SPHERICAL STRESS WAVES

The debris particles impacting the mainwall surface generate spherical dilatational stress waves in the structure. This wave propagation can be specified by the equation

$$\frac{\partial^2\phi}{\partial t^2} = c_1^2\left(\frac{\partial^2\phi}{\partial r^2} + \frac{2}{r}\frac{\partial\phi}{\partial r}\right) \tag{10}$$

where ϕ is a scalar displacement potential, c_1 is the wave velocity, r is the radius vector from the point of impact, and t is time. Particle displacement (u) is specified by the relation

$$u = \frac{\partial\phi}{\partial r} \tag{11}$$

The radial and tangential stresses are

$$\sigma_r = (\lambda+2\mu)\frac{\partial u}{\partial r} + 2\lambda\left(\frac{u}{r}\right) \tag{12}$$

and

$$\sigma_\theta = \lambda\left(\frac{\partial u}{\partial r}\right) + 2(\lambda+\mu)\left(\frac{u}{r}\right) \tag{13}$$

where λ and μ are the Lamé constants and are related to Young's modulus (E) and Poisson's ratio (ν) as follows:

$$\lambda = \frac{\nu E}{(1+\nu)(1-2\nu)} \tag{14}$$

$$\mu = \frac{E}{2(1+\nu)} \tag{15}$$

If the time-varying pressure (p) given by Equation (3) is applied to the surface of an assumed hollow hemispherical cavity of radius R_o in the target with its center at the point of impact, elastic stress waves will be generated in the structure. This mathematical model is that described by the author in Reference 9.

A solution of the wave equations, based on Blake's work, (References 10 and 11) is

$$\phi = \sum_{i=1}^{n} \frac{K(1-A\tan^2\theta)r_o}{pr(\omega_o^2+(\alpha_o-\alpha_i)^2} \left\{ - e^{-\alpha_i\tau} + e^{-\alpha_o\tau}\left[1+\left(\frac{\alpha_o-\alpha_i}{\omega_o}\right)^2\right]^{0.5} \cos\left[\omega_o\tau - \tan^{-1}\left(\frac{\alpha_o-\alpha_i}{\omega_o}\right)\right]\right\} \tag{16}$$

where

$$\tau = t - \left(\frac{r-r_o}{c_1}\right) \tag{17}$$

$$\alpha_o = \frac{c_1}{r_o}\left(\frac{1-2\nu}{1-\nu}\right) \tag{18}$$

$$\omega_o = \frac{c_1}{r_o}\left[\frac{(1-2\nu)}{1-\nu}^{0.5}\right] \tag{19}$$

5. REFLECTION AND REFRACTION AT AN INTERFACE BETWEEN TWO MEDIA

When an elastic wave of dilatation reaches a boundary between two media as is the case of the laminated mainwall considered in this study, four waves are generated. Two of these, a dilatation or longitudinal wave (RL) and a distortional or shear wave (RS), are reflected back into the first medium, and two such waves (TL) and (TS) are transmitted into the second medium (Reference 12).

At the interface there are four boundary conditions. These are that on both sides of the boundary the following quantities must be equal:

(a) The normal displacements;

(b) The tangential displacements;

(c) The normal stress;

(d) The tangential stress.

The transmitted and reflected waves and their angles with a normal to the interface are shown in Figure 8. RL, RS, TL, TS are the stress amplitudes of the waves.

The relations between the wave velocities and the angles of incidence and reflection are:

$$\frac{\sin\theta}{c_1} = \frac{\sin\Phi}{c_1} = \frac{\sin\beta}{c_1'} = \frac{\sin\theta'}{c_2} = \frac{\sin\beta'}{c_2'} \tag{20}$$

where c_1 and c_1' are the velocities of the longitudinal and shear waves in the first medium, and c_2 and c_2' are the corresponding velocities in the second medium. These velocities are given by the relation

$$c_1 = \left[\frac{E_1(1-\nu_1)}{\rho_1(1+\nu_1)(1-2\nu_1)}\right]^{0.5} \tag{21}$$

$$c_1' = \left[\frac{E_1}{2\rho_1(1+\nu_1)}\right]^{0.5} \tag{22}$$

$$c_2 = \left[\frac{E_2(1-\nu_2)}{\rho_2(1+\nu_2)(1-2\nu_2)}\right]^{0.5} \tag{23}$$

$$c_2' = \left[\frac{E_2}{2\rho_2(1+\nu_2)}\right]^{0.5} \tag{24}$$

The four boundary conditions lead to the following four equations which, together with the relations of Equations (20), may be solved for the stress wave amplitudes and their directions.

$$+\frac{\cos\theta}{\rho_1 c_1}\left[\frac{RL}{p}\right] - \frac{\sin\beta}{\rho_1 c_1'}\left[\frac{RS}{p}\right] + \frac{\cos\theta'}{\rho_2 c_2}\left[\frac{TL}{p}\right] + \frac{\sin\beta'}{\rho_2 c_2'}\left[\frac{TS}{p}\right] = +\frac{\cos\theta}{\rho_1 c_1} \tag{25}$$

$$+\frac{\sin\theta}{\rho_1 c_1}\left[\frac{RL}{p}\right] + \frac{\cos\beta}{\rho_1 c_1'}\left[\frac{RS}{p}\right] - \frac{\sin\theta'}{\rho_2 c_2}\left[\frac{TL}{p}\right] + \frac{\cos\beta'}{\rho_2 c_2'}\left[\frac{TS}{p}\right] = -\frac{\sin\theta}{\rho_1 c_1} \tag{26}$$

$$-\cos 2\beta\left[\frac{RL}{p}\right] + \sin 2\beta\left[\frac{RS}{p}\right] + \cos 2\beta'\left[\frac{TL}{p}\right] + \sin 2\beta'\left[\frac{TS}{p}\right] = +\cos 2\beta \tag{27}$$

$$+\left(\frac{c_1'}{c_1}\right)^2 \sin 2\theta \left[\frac{RL}{p}\right] + \cos 2\beta \left[\frac{RS}{p}\right] + \left(\frac{c_2'}{c_2}\right)^2 \sin 2\theta' \left[\frac{TL}{p}\right] - \cos 2\beta' \left[\frac{TS}{p}\right] = +\left(\frac{c_1'}{c_1}\right)^2 \sin 2\theta \quad (28)$$

The two materials being considered for laminated spacecraft mainwalls are polycarbonate and aluminum. Nominal values of the mechanical properties of these materials are:

Aluminum	Polycarbonate
$E = 6.9 \times 10^{11}$ dynes/cm^2	$E = 0.24 \times 10^{11}$ dynes/cm^2
$\rho = 2.68$	$\rho = 1.21$
$\nu = 0.33$	$\nu = 0.40$

The outer layer of the material is polycarbonate and the material on the inside is aluminum. The incident stress wave at the interface is assumed to have an amplitude of unity. The values of the reflected and transmitted wave amplitudes and the angles of reflection and refraction are given in Figure 9. When the velocity of propagation of the transmitted wave is greater than that of the incident wave, as in this example, there is a critical angle of incidence which makes the angle of refraction 90 degrees. This angle is approximately 22 degrees for the polycarbonate-aluminum laminate being considered. For angles of incidence greater than this, the relations that have been derived do not apply. For angles of incidence greater than the critical angle, the problem must be treated in terms of complex quantities (Reference 13, p. 38). This has not been done in this study.

If the materials are reversed so that the outer layer is aluminum and the inner material is polycarbonate, the transmitted stresses are greatly reduced. This has been demonstrated experimentally by Gehring (Reference 14, p. 474). Figure 10 gives the results for this condition. In this case there is no critical angle and therefore no limitation on the value of the incident angle. Figure 11 shows the transmitted and reflected stress amplitudes as vectors, giving a clearer picture of both and angles and amplitudes.

Although these results give a graphical comparison of the wave amplitudes they do not present the true picture when the stress waves result from the impact of fragments in the spray cloud. Assuming that the momentum distribution per unit area is proportional to $(1-6\tan^2\theta)$ as shown in Figure 2, the values of the incident, transmitted, and reflected waves will be as shown in Figure 12. These values are shown as vectors in Figure 13.

The location of the wave fronts in a polycarbonate-aluminum mainwall at times from 0 to 2.0 microseconds are shown in Figure 14 for the conditions indicated. This figure is for illustrative purposes only and does not represent actual dimensions.

6. METHOD OF STRESS ANALYSIS

In Figures 15 and 16, Y is the distance from the apparent point of origin of the debris fragments from the mainwall which is assumed to be equal to the sum of the bumper spacing, bumper thickness, and projectile diameter. The thickness of the first layer is indicated by T_1 and the thickness of the second layer by T_2. The location of any point (P) in the material is given by the coordinates x and y. The y-distance is measured from the material interface. A positive value of y indicates that the point is in the second layer of the material and a negative value indicates that it is in the first layer. For the present, only points in the second layer are being considered.

As fragments impact the mainwall it is assumed that spherical stress waves are generated but only those portions in the direction of the impacting particles which will ultimately reach point P are being considered. There are, of course, an extremely large number of stress waves in the structure, one being generated by each debris particle. These will, according to the Huygens principle, result in essentially a single wave front as shown in Figure 14. It is assumed that the material at point P will be affected by only those portions of the waves that pass through the point. A brief outline of the methods used to compute the principal stresses within the second laminate will first be described, followed by the relations and equations used in the computations. The fragments moving in the direction θ_1 will generate a wave having an amplitude of p_1 when it reaches the interface. Two waves, a longitudinal and a shear, will be reflected at the interface and two such waves will be transmitted. The longitudinal wave $(TL)_1$ will reach the point as shown in Figure 16. As was seen in Figure 13, the amplitude of the shear waves will be small compared with the longitudinal waves and their effects will be neglected. The fragments moving in the direction θ_2 will likewise generate both shear and longitudinal waves at the interface. Considering only the longitudinal wave, it will be reflected from the inner surface to point P. It has been shown (Reference 15) that the shear wave reflected from a free surface will contribute very little to the total stress. Each of the waves $(TL)_1$ and $(TRL)_2$ creates radial stresses (σ_r) and tangential stresses (σ_θ) at the point. The x and y components of stress due to each wave are computed and their combined effects are determined by superposition. From this, the maximum and minimum principal stresses and their directions are computed. This will give the stress history at that point. By considering a large number of points within the material, the stress field can be plotted for any time, as well as the maximum tensile and compressive stresses that are generated within the material.

In this analysis, the forcing function is applied to the surface of a hemispherical cavity, the radius of which is equal to or greater than the distance at which the stress wave may be considered to be elastic. The method

of determining the radius of this cavity (R_o) will be discussed later.

To simplify computations, it is assumed that the stress waves originate and travel through a homogeneous target of the second material. The imaginary cavities in which the waves originate are located so that the waves reach point P at the same time and from the same direction as if they moved along the paths shown in Figure 16.

The center of the first cavity is located at O_1 at a distance R_1 from point P.

$$R_1 = O_1P = \frac{c_2}{c_1}\left[\frac{T_1}{\cos\theta_1}\right] + \frac{y}{\cos\theta_1'} \tag{29}$$

at an angle of θ_1' (Figure 17). Its radius is (c_2R_o/c_1). This wave will have the correct amplitude if the factor $(TL)_1/p_1$ is applied. Likewise, the second wave may be assumed to originate in a cavity of radius (c_2R_o/c_1) with its center (O_2) at a distance R_2 from point P.

$$R_2 = O_2P = \frac{c_2}{c_1}\left[\frac{T_1}{\cos\theta_2}\right] + \left[\frac{2T_2-y}{\cos\theta_2'}\right] \tag{30}$$

at an angle of θ_2'. The correction factor for the wave amplitude is $(TRL)_2/p_2$.

The following values must also be computed in order to calculate the principal stresses at point P.

Values of θ_1 and θ_1' can be found by solving the two equations

$$X = (Y+T_1)\tan\theta_1 + y\tan\theta_1' \tag{31}$$

and

$$c_1/c_2 = \sin\theta_1/\sin\theta_1' \tag{32}$$

Values of θ_2 and θ_2' can be computed by solving the two relations

$$X = (Y+T_1)\tan\theta_2 + (2T_2-y)\tan\theta_2' \tag{33}$$

and

$$c_1/c_2 = \sin\theta_2/\sin\theta_2' \tag{34}$$

Values of β_1, β_1', β_2, β_2', and β_2'' are determined from the relations

$$\sin\theta_1/c_1 = \sin\beta_1/c_1' = \sin\beta_1'/c_2' \tag{35}$$

$$\sin \theta_2/c_1 = \sin \beta_2/c_1' = \sin \beta_2'/c_2' \tag{36}$$

and

$$\sin \theta_2'/c_2 = \sin \beta_2''/c_2' \tag{37}$$

The times t_1 and t_2 at which the forcing function is applied to the cavities O_1 and O_2 are

$$t_1 = \frac{Y+R_o}{\nu}\left[\frac{1}{\cos\theta_1(\cos 3\theta_1)^{0.5}} - 1\right] \tag{38}$$

and

$$t_2 = \frac{Y+R_o}{\nu}\left[\frac{1}{\cos\theta_2(\cos 3\theta_2)^{0.5}} - 1\right] \tag{39}$$

The times of arrival of the two wave fronts at point P are

$$t_{1f} = t_1 + \frac{T_1-R_o}{c_1\cos\theta_1} + \frac{2T_2-y}{c_2\cos\theta_1'} \tag{40}$$

$$t_{2f} = t_2 + \frac{T_1-R_o}{c_1\cos\theta_2} + \frac{2T_2-y}{c_2\cos\theta_2'} \tag{41}$$

Stress wave amplitudes $(TL)_1/p_1$ and $(TL)_2/p_2$ can be found by solving Equations 25, 26, 27, and 28 when the corresponding subscripts are used.

The ratio of the incident to reflected waves $(TRL)_2/(TL)_2$ at the inner surface is found by applying the conditions of zero normal and shear stresses at a free surface. This gives the relation

$$\frac{(TRL)_2}{(TL)_2} = \frac{-\sin 2\theta_2' \sin 2\beta_2'' + (c_2/c_2')^2 \cos^2 2\beta_2''}{+\sin 2\theta_2' \sin 2\beta_2'' + (c_2/c_2')^2 \cos^2 2\beta_2''} \tag{42}$$

The ratio $(TRL)_2/p_2$ may now be found

$$\frac{(TRL)_2}{p_2} = \frac{(TRL)_2}{(TL)_2} \cdot \frac{(TL)_2}{p_2} \tag{43}$$

The pressure pulse to be applied to cavity O_1 is that of Equation (3) multiplied by the factor $(TL)_1/p_1$ giving

$$F_1 = \left[\frac{(TL)_1}{P_1}\right] K(1-A \tan^2\theta_1) \left[e^{-\alpha_1(t-t_1)} - e^{-\alpha_2(t-t_1)}\right] \quad (44)$$

and the pulse to be applied to O_2 is

$$F_2 = \left[\frac{(TRL)_2}{P_2}\right] K(1-A \tan^2\theta_2) \left[e^{-\alpha_1(t-t_1)} - e^{-\alpha_2(t-t_2)}\right] \quad (45)$$

The radial and tangential components of stress at point P produced by these waves are σ_{r_1}, σ_{t_1}, σ_{r_2}, and σ_{t_2}. In order to determine the resulting stress it is necessary to resolve these stresses into their x and y components as follows

$$\sigma_{x_1} = \frac{\sigma_{r_1}+\sigma_{\theta_1}}{2} - \frac{\sigma_{r_1}-\sigma_{\theta_1}}{2} \cos 2\theta_1' \quad (46)$$

$$\sigma_{y_1} = \frac{\sigma_{r_1}+\sigma_{\theta_1}}{2} + \frac{\sigma_{r_1}-\sigma_{\theta_1}}{2} \cos 2\theta_1' \quad (47)$$

$$\tau_{xy_1} = \frac{\sigma_{r_1}-\sigma_{\theta_1}}{2} \sin 2\theta_1' \quad (48)$$

$$\sigma_{x_2} = \frac{\sigma_{r_2}+\sigma_{\theta_2}}{2} - \frac{\sigma_{r_2}-\sigma_{\theta_2}}{2} \cos 2\theta_2' \quad (49)$$

$$\sigma_{y_2} = \frac{\sigma_{r_2}-\sigma_{\theta_2}}{2} + \frac{\sigma_{r_2}-\sigma_{\theta_2}}{2} \cos 2\theta_2' \quad (50)$$

$$\tau_{xy_2} = \frac{\sigma_{r_2}-\sigma_{\theta_2}}{2} \sin 2\theta_2' \quad (51)$$

The resulting x and y components of stress at the point are then

$$\sigma_x = \sigma_{x_1} + \sigma_{x_2} \quad (52)$$

$$\sigma_y = \sigma_{y_1} + \sigma_{y_2} \quad (53)$$

$$\tau_{xy} = \tau_{xy_1} + \tau_{xy_2} \quad (54)$$

From which the principal (p and q) stresses are found

$$p = \frac{\sigma_x+\sigma_y}{2} + \left[\left(\frac{\sigma_x-\sigma_y}{2}\right)^2 + (\tau_{xy})^2\right]^{0.5} \quad (55)$$

$$q = \frac{\sigma_x+\sigma_y}{2} - \left[\left(\frac{\sigma_x-\sigma_y}{2}\right)^2 + (\tau_{xy})\right]^{0.5} \quad (56)$$

The direction of the maximum principal stress is

$$\gamma = \tfrac{1}{2}\tan^{-1}\frac{2\tau_{xy}}{\sigma_x-\sigma_y} \quad (57)$$

7. PROCEDURE FOR COMPUTING THE STRESS HISTORY AT A POINT IN THE SECOND LAMINATE

1. Specify values of the constants E_1, E_2, ρ_1, ρ_2, ν_1, ν_2, m, v, M, Y, T_1, T_2, R_o, A, B, n, α_1, α_2, Δt, x, and y.
2. Compute K - Equation (8).
3. Stress wave velocities c_1, c_1', c_2, and c_2' - Equations (21), (22), (23), (24).
4. Compute angles θ_1 and θ_1' - Equations (31), (32).
5. Compute angles θ_2 and θ_2' - Equations (33), (34).
6. Compute angles β_1 and β_1' - Equation (35).
7. Compute angles β_2 and β_2' - Equation (36).
8. Compute angle β_2'' - Equation (37).
9. Compute the time t_1 - Equation (38).
10. Compute the time t_2 - Equation (39).
11. Compute the time t_{1f} - Equation (40).
12. Compute the time t_{2f} - Equation (41).
13. Compute the cavity radius $R_{o1} = R_{o2} = c_2R_o/c_1$ (page 9).
14. Compute the distance R_1 - Equation (29).
15. Compute the distance R_2 - Equation (30).
16. Compute the ratios $(TL)_1/p_1$ and $(TL)_2/p_2$ - Equations (25), (26), (27), (28).
17. Compute the ratio $(TRL)_2/(TL)_2$ - Equation (42).
18. Compute the ratio $(TRL)_2/p_2$ - Equation (43).

19. Compute the forcing function F_1 - Equation (44).

20. Compute the stresses σ_{r_1} and σ_{θ_1} at time increments of Δt starting at time t_{1f} - Equations (12), (13).

21. Compute the x, y components σ_{x_1}, σ_{y_1}, and τ_{xy_1} - Equations (46), (47), (48).

22. Compute the forcing function F_2 - Equation (45).

23. Compute the stresses σ_{r_2} and σ_{θ_2} at time increments of Δt starting at time t_{2f} - Equations (12, (13).

    NOTE: The stresses of step 20 must be computed for the same times of step 23 after time t_{2f}.

24. Compute the x, y components σ_{x_2}, σ_{y_2}, and τ_{xy_2} - Equations (49), (50), (51).

25. Compute the values of σ_x, σ_y, and τ_{xy} - Equations (52), (53), (54).

26. Compute values of the principal stresses, p and q - Equations (55), (56).

27. Compute the direction of the maximum principal stress, γ - Equation (57).

8. EXPERIMENTAL DATA

As the method employed in this study is semi-empirical or quasi-theoretical in nature, some experimental data must be used if actual values of stress rather than relative values are to be computed. This experimental information was supplied by the NASA Langley Research Center (Reference 16). The information was for six targets, four of which were solid 2024-T3 aluminum targets and two of which were polycarbonate-aluminum laminated targets. The data supplied are given in Table I.

A search of the literature failed to reveal any significant information about the dynamic strength of this material. The peak tensile stress for incipient spall failure in 6061-T6 aluminum was given as 15 kilobars for a pulse duration of 0.1 microsecond in Reference 17, p. 398. The static tensile strength of 2024-T3 is about 50 percent greater than that of 6061-T6; however, this is perhaps somewhat greater than the dynamic strength ratio of these materials. It is believed that a dynamic tensile strength of 20 kilobars or about 300,000 psi is a realistic value and will be used in this study.

Although a stress criteria for fracture is assumed in this analysis, it is realized that fracture is probably time-dependent and that the strain-rate would perhaps be a more significant factor to consider.

9. TENSILE STRESSES IN SOLID ALUMINUM TARGETS

Because of the small size of the individual particles in the debris cloud, it is believed that the shock waves generated will decay into elastic waves within a very short distance. Because of this, it is concluded that the value of R_o should be small, perhaps a fraction of a millimeter. In this study the value of R_o will be varied from 0.25 to 0.50 mm in order to find the value that will give results that are in agreement with the experiments.

Another factor that will affect the values of the computed stress is the shape of the forcing function applied to the cavity radius. The forward momentum of this forcing function will be equal to that of the impacting debris but its amplitude will depend upon the rise and decay times of the pulse. Rise times of 0.05 and 0.10 microsecond will be investigated and the ratio of the decay to the rise time will be assumed to have a value of five.

The method given for the analysis of stresses in laminated targets may be used for solid targets by assigning a value of zero to T_1.

The target dimensions are those given in Table I for shots 1, 2, 3, and 4. The value of Y is 1.00 cm, the sum of the projectile diameter (0.153 cm), the bumper thickness (0.043 cm), and the bumper spacing (0.800 cm). As the projectile velocities are approximately the same, an average of 7.85 km/sec is used.

There are three possible causes of tensile stress, any of which may be the maximum. These are illustrated in Figure 18. There will be tangential tensile stresses near the front surface of the target. The radial fractures seen extending out from the crater in transparent plastic targets are produced by these stresses. There will be radial tensile stresses produced by the tail of the forward-moving wave. These are usually of relatively small amplitude. There will be the radial tensile stresses caused by the reflected compression wave. These stresses are the cause of internal cracks approximately parallel to the rear surface or the spallation of the target's rear surface. The maximum of these tensile stresses is always considered at any point.

Figure 19 shows the maximum tensile stress along the y-axis of the four solid aluminum targets using a forcing function of 0.05-microsecond rise time. The effect of the value selected for R_o is apparent. If R_o is assumed to be 0.050 cm, the material must have a dynamic tensile strength of approximately 114 kilobars as shown because target No. 3 failed by spallation and target No. 4 did not fail. Likewise, for a value of R_o of 0.0375, the tensile strength must be about 80 kilobars; and for R_o = 0.025, the strength must be about 50 kilobars.

Changing the decay constants so that the forcing function has a rise time of 0.10 microsecond, a value of 0.050 cm for R_o would require a dynamic tensile strength of about 54 kilobars. Decreasing the cavity radius to 0.0375 cm decreases the required strength to about 37 kilobars. When R_o has a value of 0.025 cm the material tensile strength must be approximately 20 kilobars, the estimated dynamic tensile strength of the target material, 2024-T3 aluminum. As seen from Figure 20, there would be no failure in target No. 4; there would be a slight spall in target No. 3; a larger spall would occur in target No. 2; and the fracture strength would be exceeded throughout target No. 1 except near the rear surface. The momentum trapped between the spall fracture and the rear surface where the normal stress is always zero would undoubtedly cause complete penetration as observed in the experimental target. This model seems to give results that are in complete agreement with the experimental observations and the estimated dynamic tensile strength of the material. A summary of the analytical and experimental results for these four aluminum targets is given in Figure 21. The radial and tangential components of the stress waves in target No. 2 for various times are shown in Figure 22.

The values of tensile stresses shown in the previous figures were for points along the target axis. Numerical values of the maximum stresses computed for points throughout these four targets are given in Tables II, III, IV, and V. The three causes of the tensile stresses are indicated on these tables. The heavy lines enclose all values exceeding the dynamic strength of 20 kilobars. Data from these tables have been plotted in Figure 23. The lateral extent of the area in which the stresses exceed the critical tensile strength of the material can be determined by following the 20-kilobar contour.

This analysis should predict failure of the material but does not describe it. If these targets had been some plastics the fractured area would probably be the entire area in which the fracture strength was exceeded (Reference 18). In aluminum targets, however, the fracture would appear as an internal crack following the portion of the 20-kilobar contour near the rear surface of the target (inner surface of the spacecraft mainwall). A part of the stress wave would be trapped between this fracture and rear surface producing a bulge or a rupture of the material. Also, this fracture would act as a new free surface for the tail of the pressure pulse, which, upon reflection from the fracture, might create additional internal cracks in the target (References 9 and 19).

10. TENSILE STRESSES IN LAMINATED POLYCARBONATE-ALUMINUM TARGETS

The relations given in Section 5 for the reflection and transmission of stress waves at an interface between two media were based upon a perfect bond between the two materials and no loss of energy at the interface. If there is perfect contact between the two materials but no bond, then compression waves will be transmitted but no tensile components can pass from the first material into the second. If there is not perfect contact between the materials or if

the dimensions of any voids between the materials are unknown, then a correlation between the computed stress and the observed fracture is impossible. Unfortunately, the two experimental targets Nos. 5 and 6 fit the last description. This obviously results in a more efficient spacecraft mainwall than if they had been perfectly bonded unless such a bond is needed for structural reasons. It would have perhaps been even more efficient if the two materials had been separated by some porous filler material. Summers and Nysmith (Reference 2) report that tests have indicated that low-density fillers such as polyurethane foam, glass wool, or aluminum honeycomb, can improve the effectiveness of a meteoroid bumper in protecting a space structure. DiBattista and Humes (Reference 20) have also shown that laminated mainwalls are superior to solid mainwalls in retarding spallation and penetration failure.

A search of the literature failed to reveal any information about the momentum multiplication associated with high-velocity impact of polycarbonate targets. If it is assumed that the momentum multiplication factor for the impact of the polycarbonate first layer and the cavity radius are the same as for the debris-aluminum impacts, the computed stresses developed in the aluminum would have been sufficient to rupture both the experimental targets. There was, however, no failure in target No. 6, but there was penetration failure of target No. 5.

One must conclude that the maximum tensile stress in the second layer of target No. 6 did not exceed the dynamic strength of 20 kilobars. If the transmitted pressure wave amplitudes in the experimental targets were only 20 percent of that transmitted through a perfectly bonded laminate, the computed stresses along the axis of the aluminum second layer would be approximately as shown in Figures 24 and 25. The stress distributions throughout these targets are shown in Figure 26.

11. EFFECTS OF BUMPER-MAINWALL SPACING

The tensile stresses were computed for polycarbonate-aluminum targets where $T_1 = T_2 = 0.127$ cm, for bumper spacings of 0.4, 0.8, and 1.2 cm. The results shown in Figure 27 indicate that for a spacing of 0.4 cm the target would be damaged extensively, perhaps perforated; that for a spacing of 0.8 cm there would probably be a slight internal fracture; and that there would be no damage for a spacing of 1.2 cm. As would be expected from the relations given in Equation (8), the maximum tensile stress varies approximately inversely as the square of the distance between the bumper and the mainwall.

12. EFFECT OF VARYING LAMINATION THICKNESSES KEEPING THE MAINWALL WEIGHT CONSTANT

Computations were made of the maximum tensile stresses in the aluminum laminate of a polycarbonate-aluminum target, keeping the total weight equal to

that of the 0.318-cm solid aluminum target of shot No. 3. The results are given in Figure 28 for three combinations of T_1 and T_2. It appears that the larger the ratio T_1/T_2, the more resistant the mainwall would be to meteoroid impact. There is, of course, some limiting value to this ratio because of structural requirements.

13. CONCLUSIONS

All computed values and conclusions have been based on a 2017-T4 aluminum projectile and a 2024-T3 aluminum bumper. Applications to other materials should be made with caution.

A bumper-protected polycarbonate-aluminum mainwall with no bonding between the two materials will increase the meteoroid-impact resistance of a structure. It appears that such a laminated mainwall will afford the same resistance to high-velocity impact as a solid aluminum structure weighing more than twice as much. Bonding of the two materials would result in greater damage and the use of a porous filler between the materials would probably result in even less structural damage. A much greater resistance to penetration would be achieved if it were possible to make the outer laminate of aluminum and the inner one of polycarbonate.

The conclusion that the amplitudes of the stress waves transmitted from the first to the second laminate of the experimental shots were approximately 20 percent of that transmitted through a perfectly bonded laminate was based upon the very unlikely assumptions that the momentum multiplication factor for aluminum-polycarbonate impact is the same as for aluminum-aluminum impact and that the cavity radius, R_o, is the same for the two materials.

It is suggested that a series of carefully controlled experiments be conducted for impacts in both bonded and unbonded laminates. The momentum multiplication factor for debris-polycarbonate impact should be determined.

REFERENCES

1. Whipple, F. L., "Meteoritic Phenomena and Meteorites," Physics and Medicine of the Upper Atmosphere, edited by C. S. White and O. O. Benson, Jr., University of New Mexico Press, 1952, p. 137.

2. Summers, James L. and Nysmith, C. Robert, "The Resistance of Composite Space Structures to Hypervelocity Impact," AIAA Fifth Annual Structures and Materials Conference Proceedings, 1964, p. 386.

3. Turpin, William C., "Hypervelocity Perforation Mechanics of Thin Metal Plates," Technical Report AFML-TR-69-203, Wright-Patterson Air Force Base, Ohio (July 1969).

4. Rosenblatt, M., Kreyenhagen, K. N., and Romine, W. D., "Analytical Study of Debris Clouds Formed by Hypervelocity Impacts on Thin Plates," Technical Report AFML-TR-68-266, Wright-Patterson Air Force Base, Ohio (December 1968).

5. Maiden, C. J. and McMillan, A. R. and Sennett III, R. E., "Thin Sheet Impact," NASA CR-295 (September 1965).

6. Madden, Richard, "Ballistic Limit of Double-Walled Meteoroid Bumper Systems," NASA TN D-3916 (April 1967).

7. Swift, H. F. and Prater, R. F., "Simulation of High Velocity Impacts On Thin Targets," Technical Report AFML-TR-68-88, Wright-Patterson Air Force Base, Ohio (May 1968).

8. Cunningham, John H., "Momentum Distribution in the Debris Cloud Produced by Hypervelocity Perforation of Thin Plates," Technical Report AFML-TR-68-174, Wright-Patterson Air Force Base, Ohio (July 1968).

9. Kinslow, Ray, "Properties of Spherical Stress Waves Produced by Hypervelocity Impact," AEDC-TDR-63-197 (AD421578), October 1963.

10. Blake, F. G., Jr., "Spherical Wave Propagation in Solid Media," Journal of the Acoustical Society of America, Vol. 24, No. 2, March 1952, pp. 211-215.

11. Allen, William A. and Goldsmith, Werner, "Elastic Description of a High-Amplitude Spherical Pulse in Steel," Journal of Applied Physics, Vol. 26, No. 1, January 1955, pp. 69-74.

12. Ewing, W. Maurice, Jardetzky, Wenceslas S., and Press, Frank, Elastic Waves in Layered Media, McGraw-Hill, 1957.

13. Brekhovskikh, Leonid M., Waves in Layered Media, Academic Press, 1960.

14. Gehring, Jr., John W., "Engineering Considerations in Hypervelocity Impact," High-Velocity Impact Phenomena, edited by Ray Kinslow, Academic Press, 1970.

15. Wilkins, James Robert, "Dynamic Analysis of Double Layered Materials," Master's Thesis, Tennessee Technological University, December 1971.

16. DiBattista, John D., Private correspondence.

17. Burke, John J. and Weiss, Volker, eds., Shock Waves and Mechanical Properties of Solids, Proceedings of the Seventeenth Sagamore Army Materials Research Conference, Syracuse University Press, 1971.

18. Kinslow, Ray, "Observations of Hypervelocity Impact of Transparent Plastic Targets," AEDC-TDR-64-49 (AD438947), May 1964.

19. Kinslow, Ray, "Properties of Reflected Stress Waves," AIAA Paper No. 69-363, 1969.

20. DiBattista, J. D., and Humes, D. H., "Multimaterial Lamination as a Means of Retarding Penetration and Spallation Failure in Plates," NASA TN D-6989 (November 1972).

TABLE I.

EXPERIMENTAL DATA

Experimental Shot Number	1	2	3	4	5	6
Projectile: Material	← Aluminum 2017-T4 →					
Diameter (cm)	← 0.153 cm →					
Velocity (km/sec)	7.75	7.84	7.95	7.85	7.69	7.87
Bumper: Material	← Aluminum 2024-T3 →					
Thickness (cm)	← 0.043 cm →					
Spacing (cm)	← 0.8 cm →					
Mainwall: First Laminate	None	None	None	None		
Material					Polycarbonate	Polycarbonate
Thickness (cm)					0.076 cm	0.152 cm
Second Laminate						
Material	← Aluminum 2024-T3 →					
Thickness (cm)	0.162 cm	0.208 cm	0.318 cm	0.361 cm	0.086*	0.086*
Results	Penetration Failure	Spallation Failure	Spallation Failure	No Failure	Penetration Failure	No Failure

Note: *Two sheets of equal thickness.

TABLE II.

COMPUTED MAXIMUM TENSILE STRESS (KILOBARS) - SHOT NO. 1

Y (inches/cm)	X (inches/cm)			
	0.0/0.0	0.05/0.127	0.10/0.254	0.15/0.380
0.015/0.038	121.0*	98.8*	49.0*	
0.020/0.051	67.4*	55.9*	30.8*	
0.025/0.0637	44.1*	37.5*	22.4*	
0.030/0.0765	32.2*	27.9*	17.7*	
0.035/0.089		22.1*	17.2***	
0.040/0.101	22.3***	23.1***	23.4***	
0.045/0.114	34.0***	32.7***	26.2***	13.3***
0.050/0.127	40.0***	35.4***	24.4***	10.4***
0.055/0.139	33.0***	28.1***	17.2***	6.82***
0.060/0.152	14.3***	11.7***	6.74***	3.94***

NOTES FOR TABLES II THROUGH V

*Tangential tensile stress near the target's front surface.

**Radial tensile stress produced by the forward-moving wave.

***Radial tensile stress caused by the reflected wave.

TABLE III.

COMPUTED MAXIMUM TENSILE STRESS (KILOBARS) - SHOT NO. 2

Y (inches/cm)	X (inches/cm)			
	0.0/0.0	0.05/0.127	0.10/0.254	0.15/0.380
0.015/0.038	121.3*	98.5*	49.0*	
0.020/0.0508	67.3*	56.0*	30.8*	
0.025/0.0635	41.5*	37.4*	22.4*	
0.030/0.076	32.2*	27.9*	17.7*	
0.035/0.089		22.0*	14.6*	
0.040/0.104	20.6*	18.2*	13.0**	
0.045/0.114	17.3*	15.7**	12.6**	
0.050/0.127	16.2**	15.2**	12.2**	8.3*
0.055/0.140	15.5**	14.6**	14.6***	14.3***
0.060/0.153	21.5***	20.9***	19.6***	15.0***
0.065/0.165	29.6***	27.7***	22.6***	13.9***
0.070/0.178	31.8***	29.0***	20.9***	11.2***
0.075/0.191	24.4***	21.5***	14.2***	7.0***
0.080/0.204	7.9***	6.6***	4.2***	3.06***

TABLE IV.

COMPUTED MAXIMUM TENSILE STRESS (KILOBARS) - SHOT NO. 3

Y (inches/cm)	X (inches/cm)			
	0.0/0.0	0.05/0.127	0.10/0.254	0.15/0.380
0.015/0.038	121.3*	98.5*	49.0*	
0.020/0.0508	67.3*	56.0*	30.8*	
0.025/0.0635	41.5*	37.4*	22.4*	
0.030/0.076	32.2*	27.9*	17.7*	
0.035/0.089	25.0*	22.0*	14.6*	
0.040/0.104	20.6*	18.2*	13.0**	
0.045/0.114	17.3*	15.7**	12.5**	
0.050/0.127	16.2**	15.2**	12.2**	8.35*
0.055/0.140	15.5**	14.6**	11.7**	8.1 **
0.060/0.153	14.8**	13.9**	11.2**	7.86**
0.065/0.165	14.1**	13.2**	10.8**	7.66**
0.070/0.178	13.4**	12.6**	10.3**	7.45**
0.075/0.197	12.7**	12.0**	9.9**	7.25**
0.080/0.204	12.1**	11.4**	9.6**	7.15**
0.085/0.219	11.5**	10.9**	9.3**	6.93**
0.090/0.228	11.1**	10.5**	8.95**	6.75**
0.095/0.241	10.6**	10.0**	8.6 **	6.68**
0.100/0.254	12.1***	11.6***	11.0***	10.4 ***
0.105/0.267	16.9***	16.3***	15.0***	12.4 ***
0.110/0.279	21.4***	20.2***	16.9***	12.4 ***
0.115/0.292	20.6***	19.0***	15.1***	10.1 ***
0.120/0.304	12.8***	11.7***	8.65***	5.45***

TABLE V.

COMPUTED MAXIMUM TENSILE STRESS (KILOBARS) - SHOT NO. 4

Y (inches/cm)	X (inches/cm)			
	0.0/0.0	0.05/0.127	0.10/0.254	0.15/0.380
0.015/0.038	121.3*	98.5*	49.0*	
0.020/0.0508	67.3*	56.0*	30.8*	
0.025/0.0635	41.5*	37.4*	22.4*	
0.030/0.076	32.2*	27.9*	17.7*	
0.035/0.089	25.0*	22.0*	14.6*	
0.040/0.104	20.6*	18.2*	13.0**	
0.045/0.114	17.3*	15.7**	12.5**	
0.050/0.127	16.2**	15.2**	12.2**	8.35*
0.055/0.140	15.5**	14.6**	11.7**	8.1 **
0.060/0.153	14.8**	13.9**	11.2**	7.86**
0.065/0.165	14.1**	13.2**	10.8**	7.66**
0.070/0.178	13.4**	12.6**	10.3**	7.45**
0.075/0.197	12.7**	12.0**	9.9**	7.25**
0.080/0.204	12.1**	11.4**	9.6**	7.15**
0.085/0.219	11.5**	10.9**	9.3**	6.93**
0.090/0.228	11.1**	10.5**	8.95**	6.75**
0.095/0.241	10.6**	10.0**	8.6 **	6.68**
0.100/0.254	10.1**	9.65**	8.3 **	6.47**
0.105/0.267	9.75**	9.3 **	8.0 **	6.33**
0.110/0.279	9.35**	8.9 **	7.8 **	6.2 **
0.115/0.292	9.6 ***	9.3 ***	8.53***	6.06**
0.120/0.304	13.0 ***	12.8 ***	12.1 ***	
0.125/0.318	17.5 ***	17.0 ***	15.0 ***	12.1 ***
0.130/0.330	19.3 ***	18.1 ***	15.1 ***	10.9 ***
0.135/0.343	14.9 ***	13.7 ***	10.9 ***	7.4 ***
0.140/0.356	4.86***	4.4 ***	3.26***	2.33***

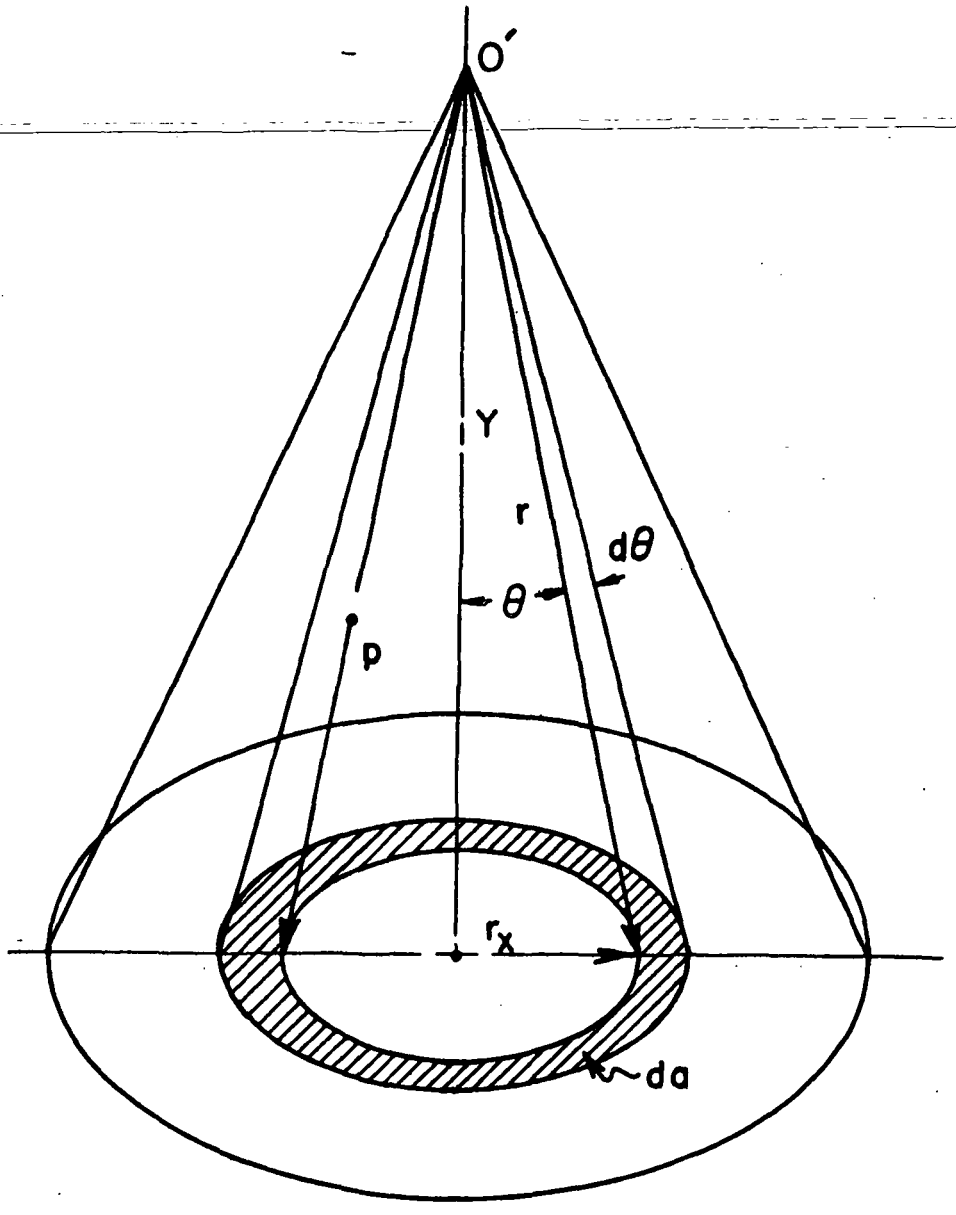

Figure 1. Coordinates Used in Debris Cloud Analysis

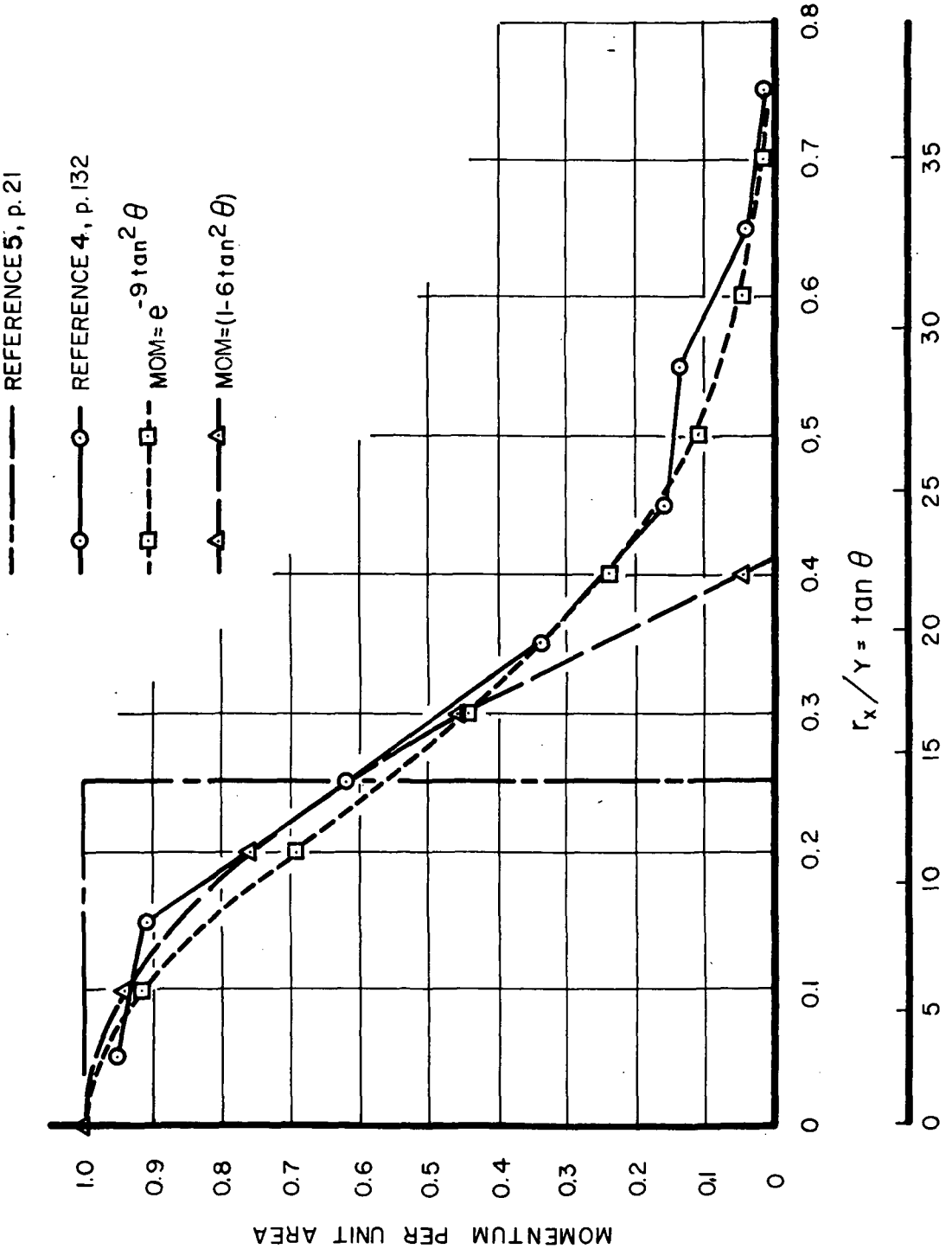

Figure 2. Debris Momentum

(From Reference 8, p. 3)

Figure 3. Photograph of Debris Cloud

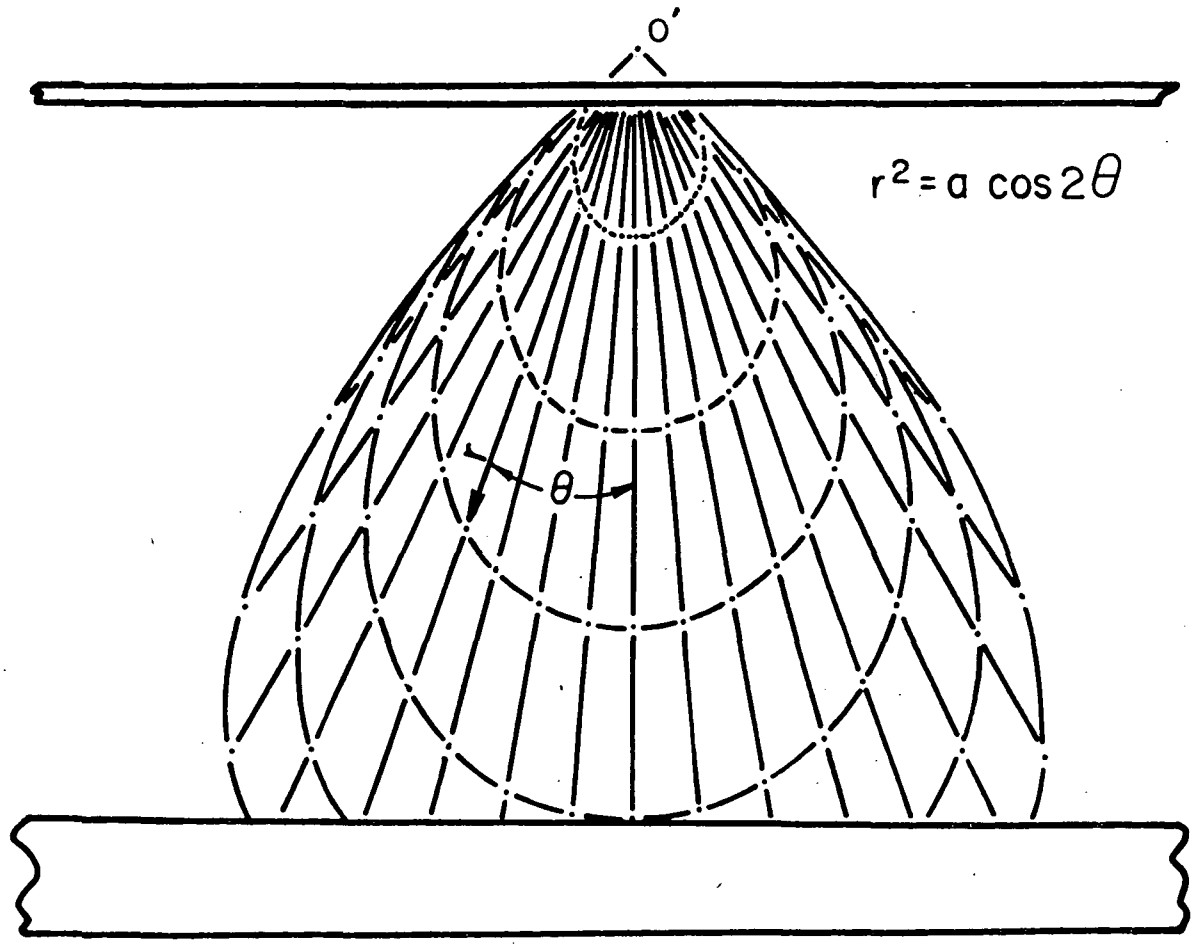

Figure 4. Lemniscates of Bernoulli

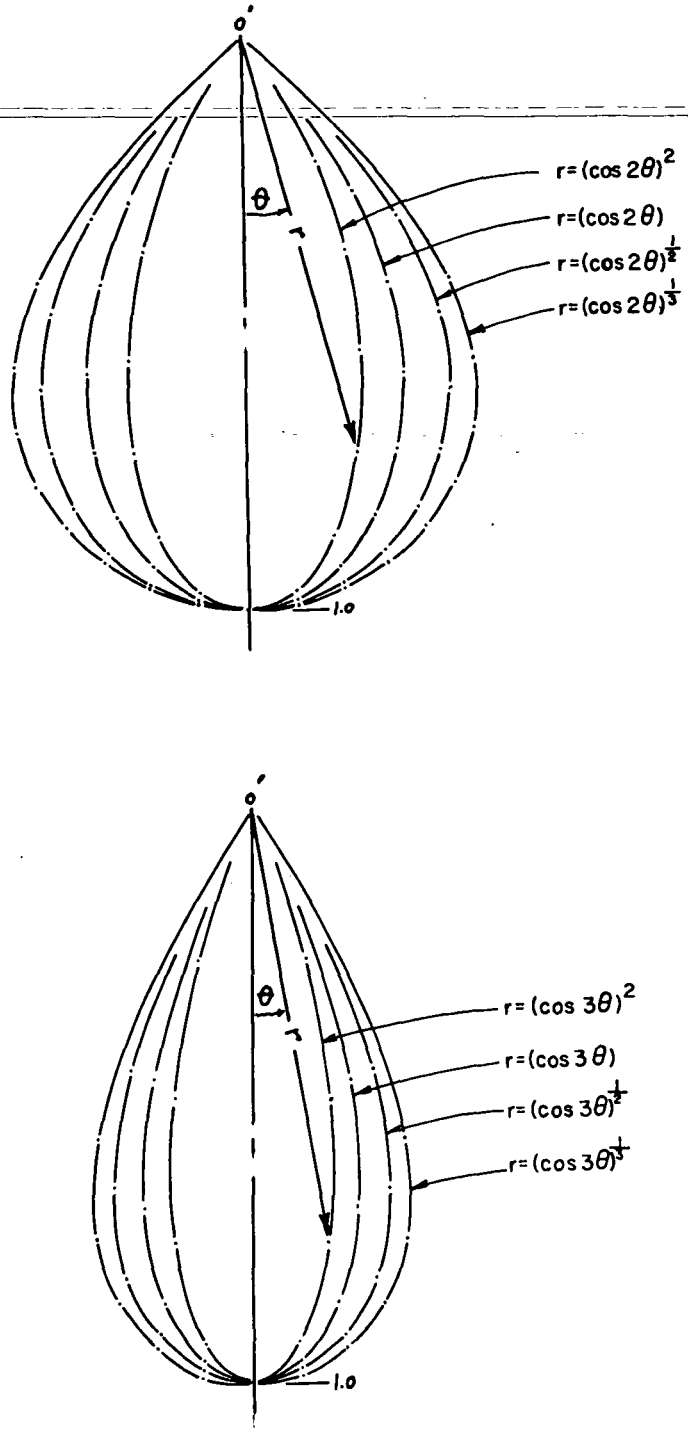

Figure 5. Various Modifications of the Lemniscate

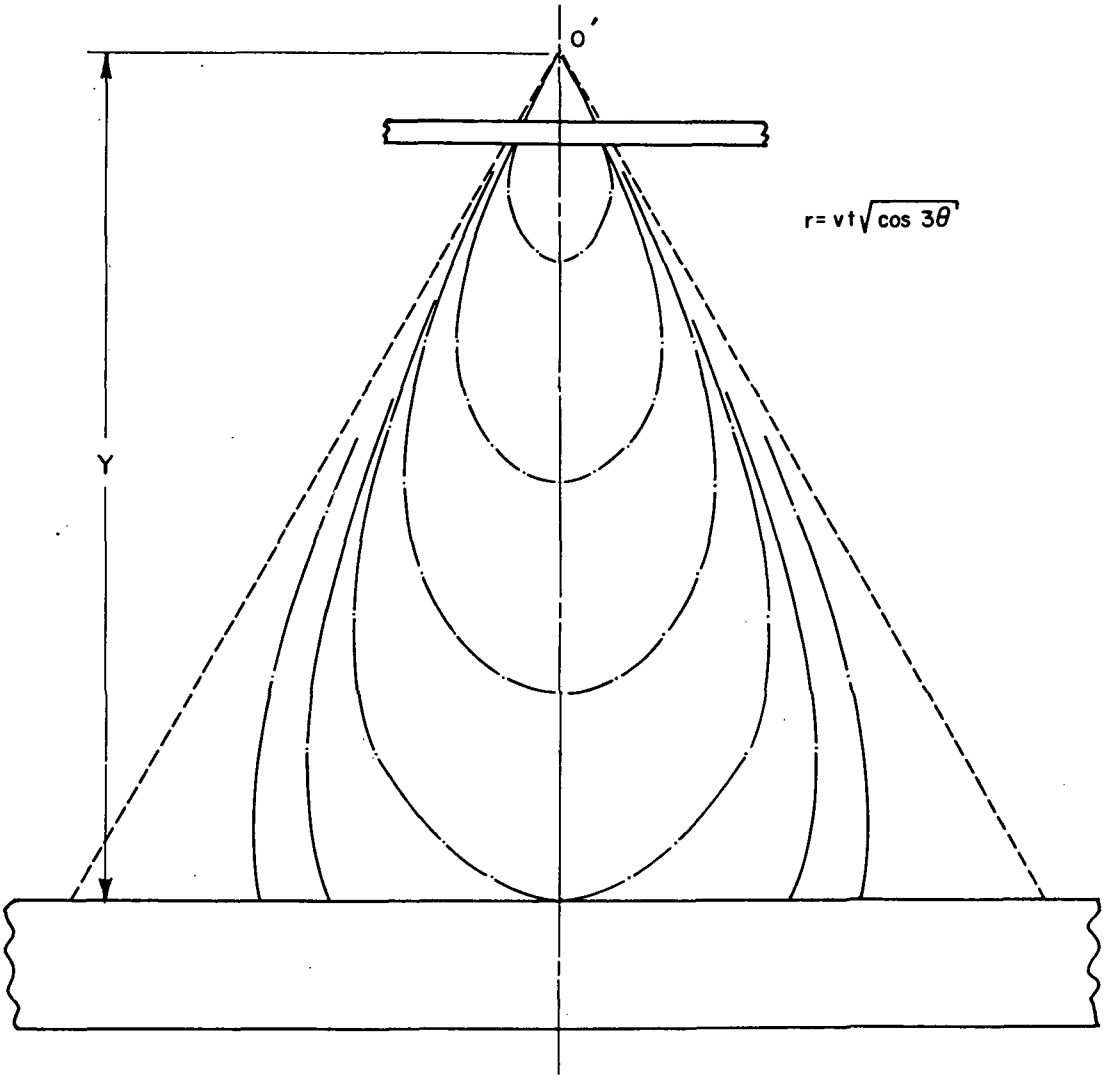

Figure 6. Debris Cloud Profiles

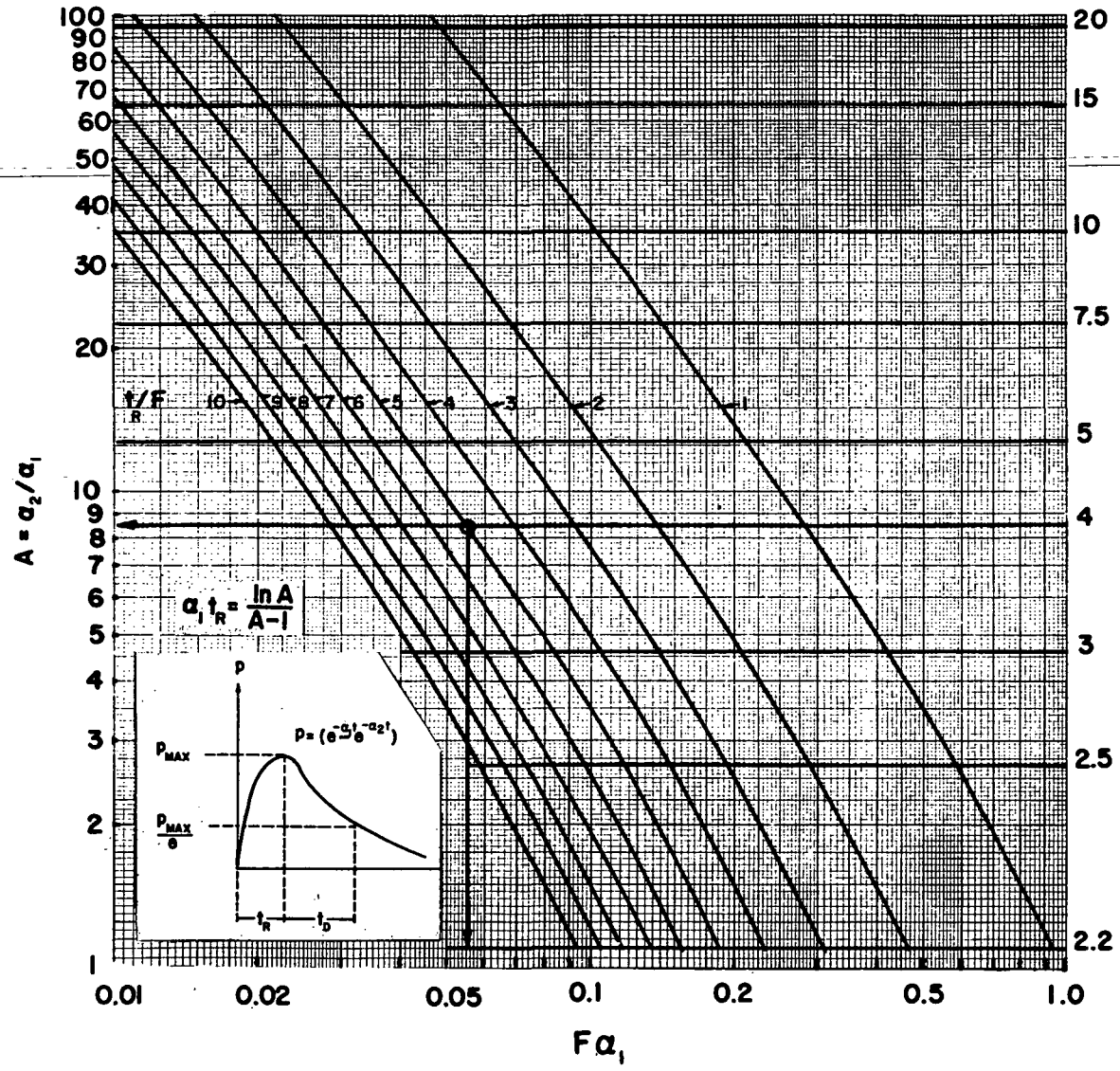

Example: Required a function that will reach a maximum stress in 0.5 microsecond and then decay to a value of 1/e of the maximum in 2.0 microseconds. To use the chart, F = 0.10 and $t_D/t_R = 4$. Locate the point shown at $t_R/F = 5$ and $t_D/t_R = 4$. On the bottom scale read $F\alpha_1 = 0.055$, giving $\alpha_1 = 0.55$, and on the scale at left read A = 8.5, giving $\alpha_2 = 4.67$.

Figure 7. Chart for Determining Decay Constants

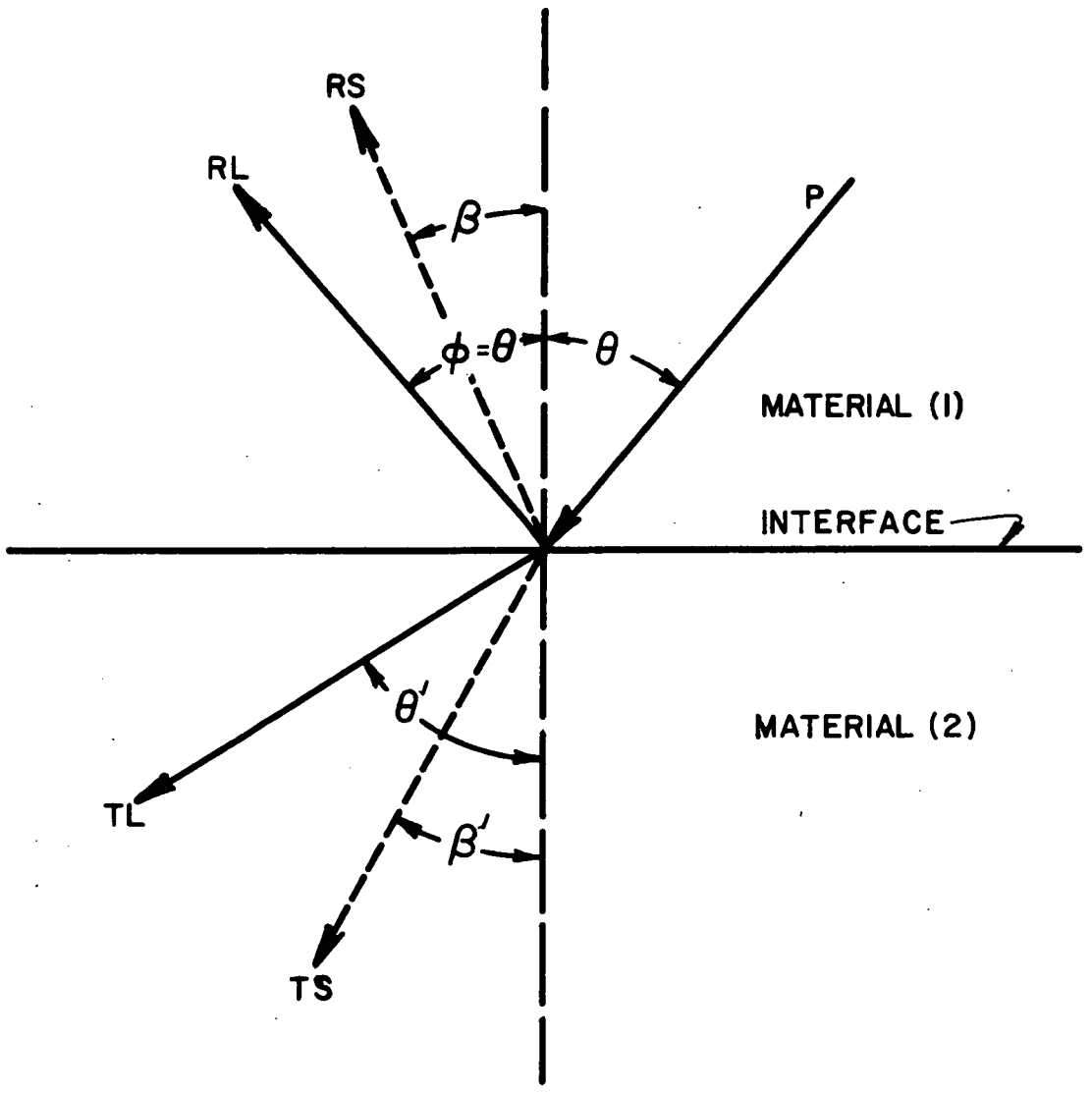

Figure 8. Transmitted and Reflected Waves at an Interface

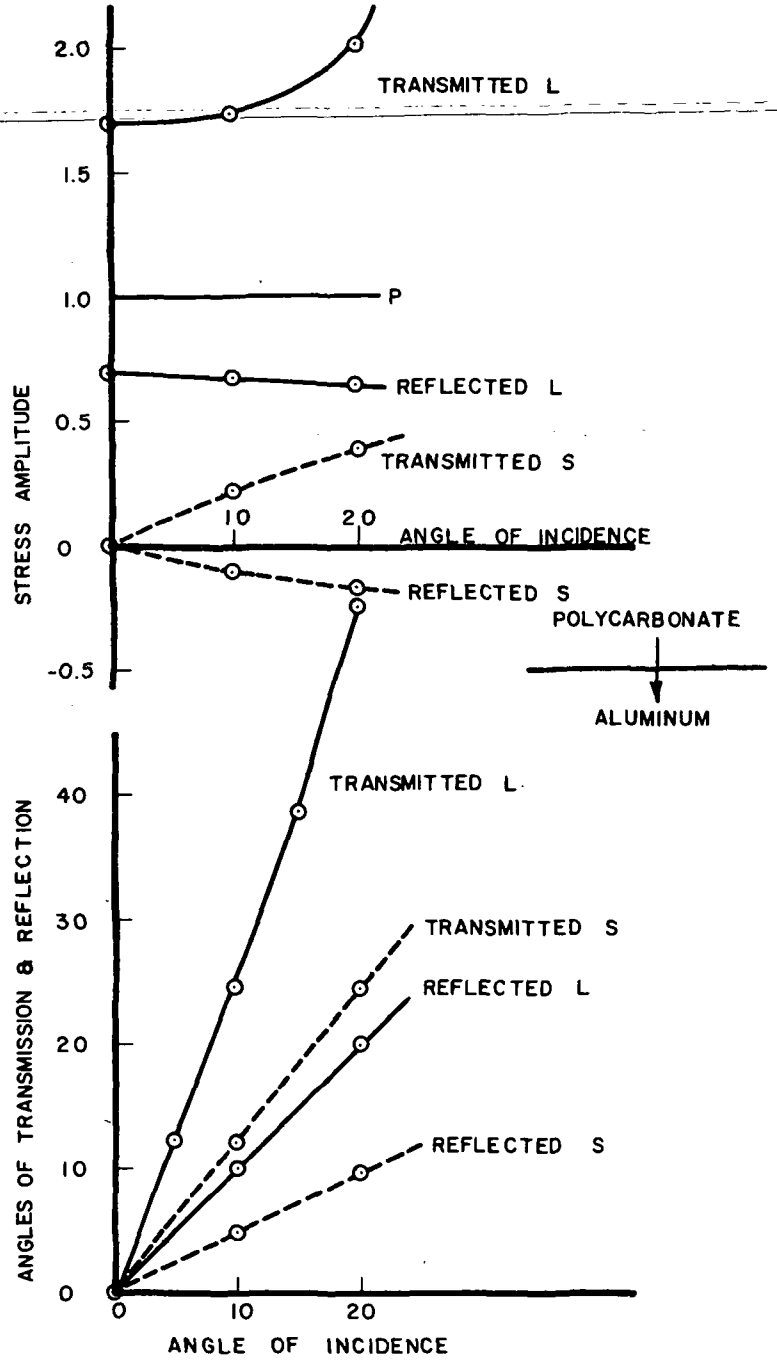

Figure 9. Stress Waves at an Interface - - Polycarbonate → Aluminum (p = 1.0)

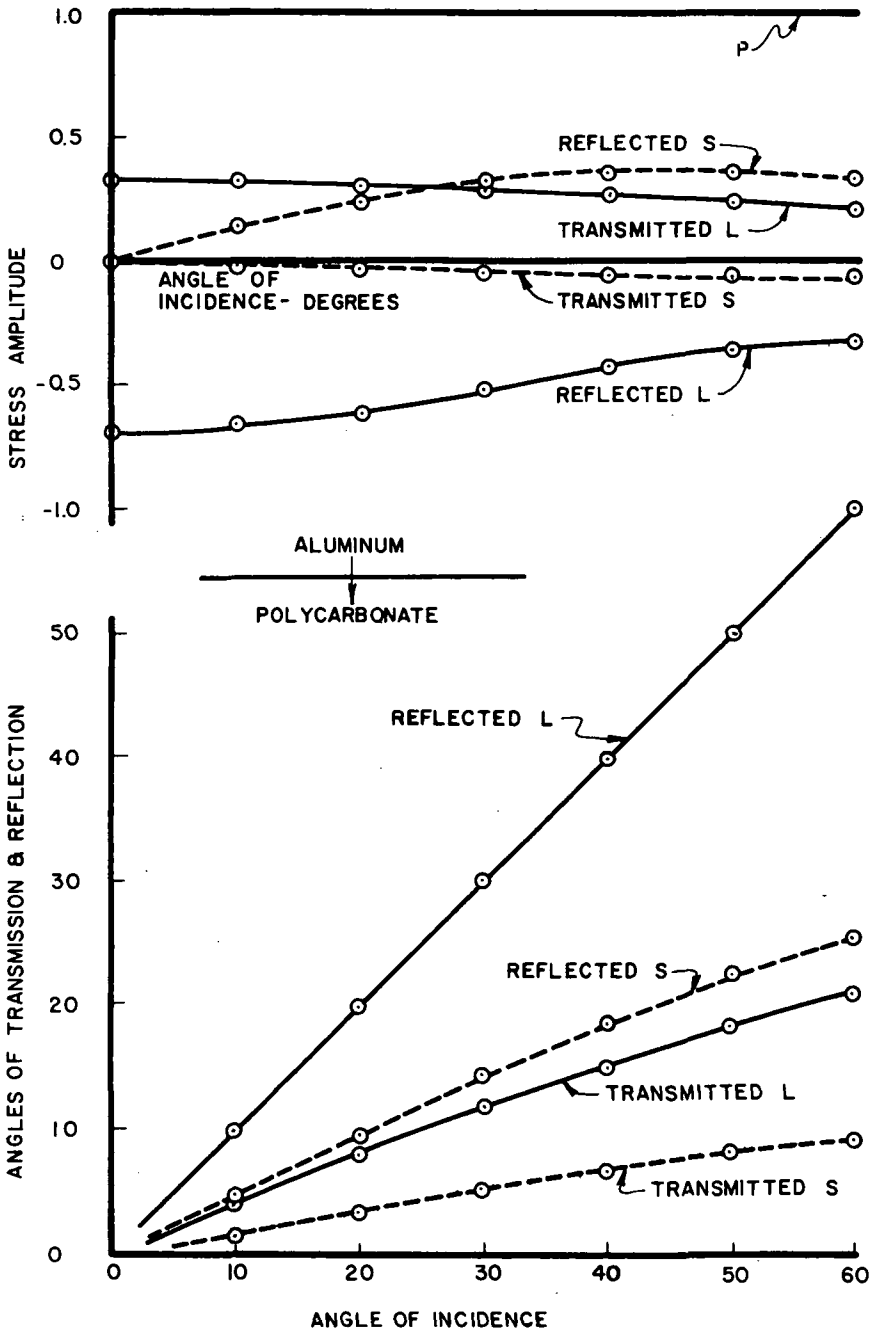

Figure 10. Stress Waves at an Interface - - Aluminum ⟶ Polycarbonate (p = 1.0)

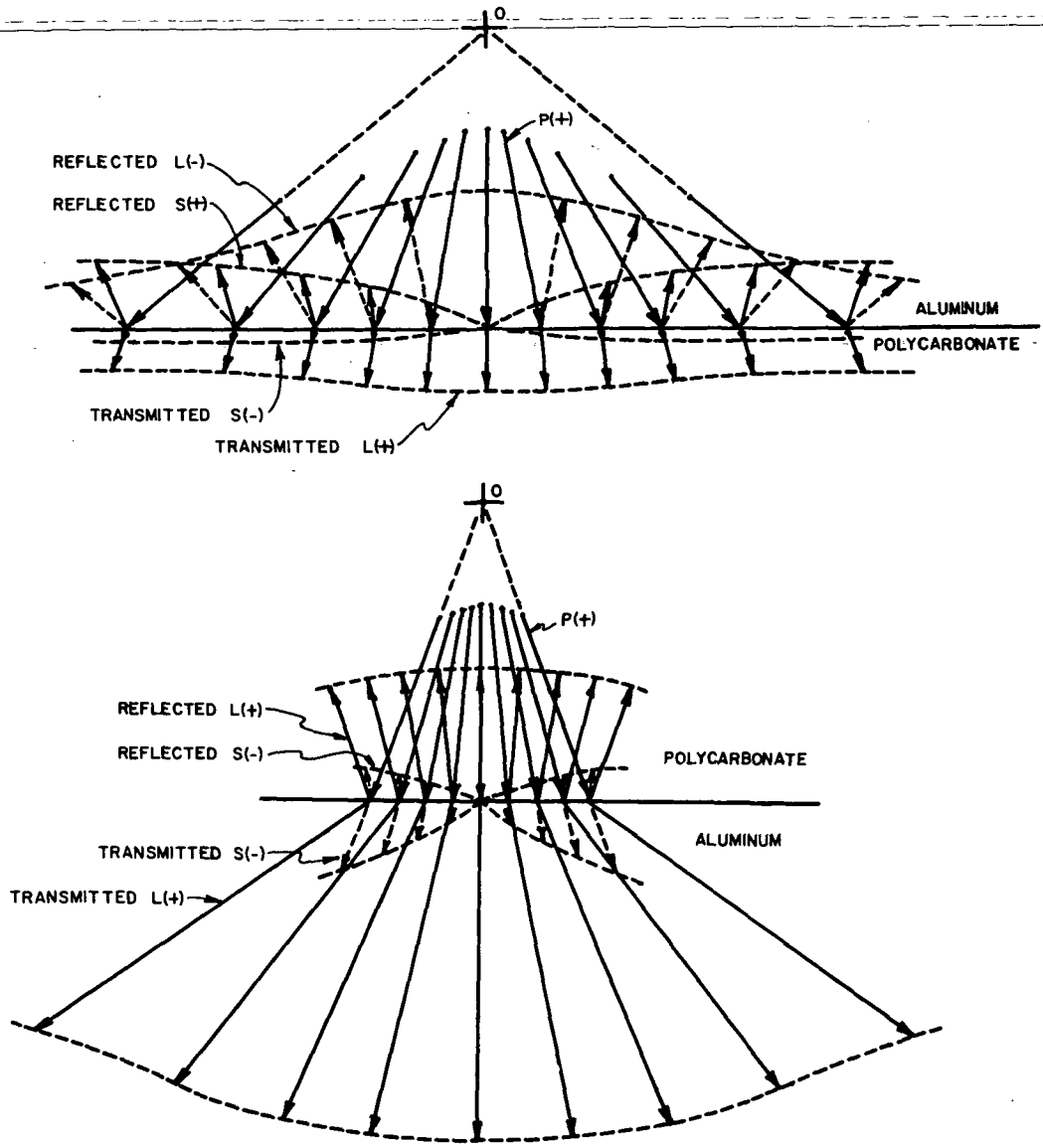

Figure 11. Vector Representation of Transmitted and Reflected Stress Waves ($p = 1.0$)

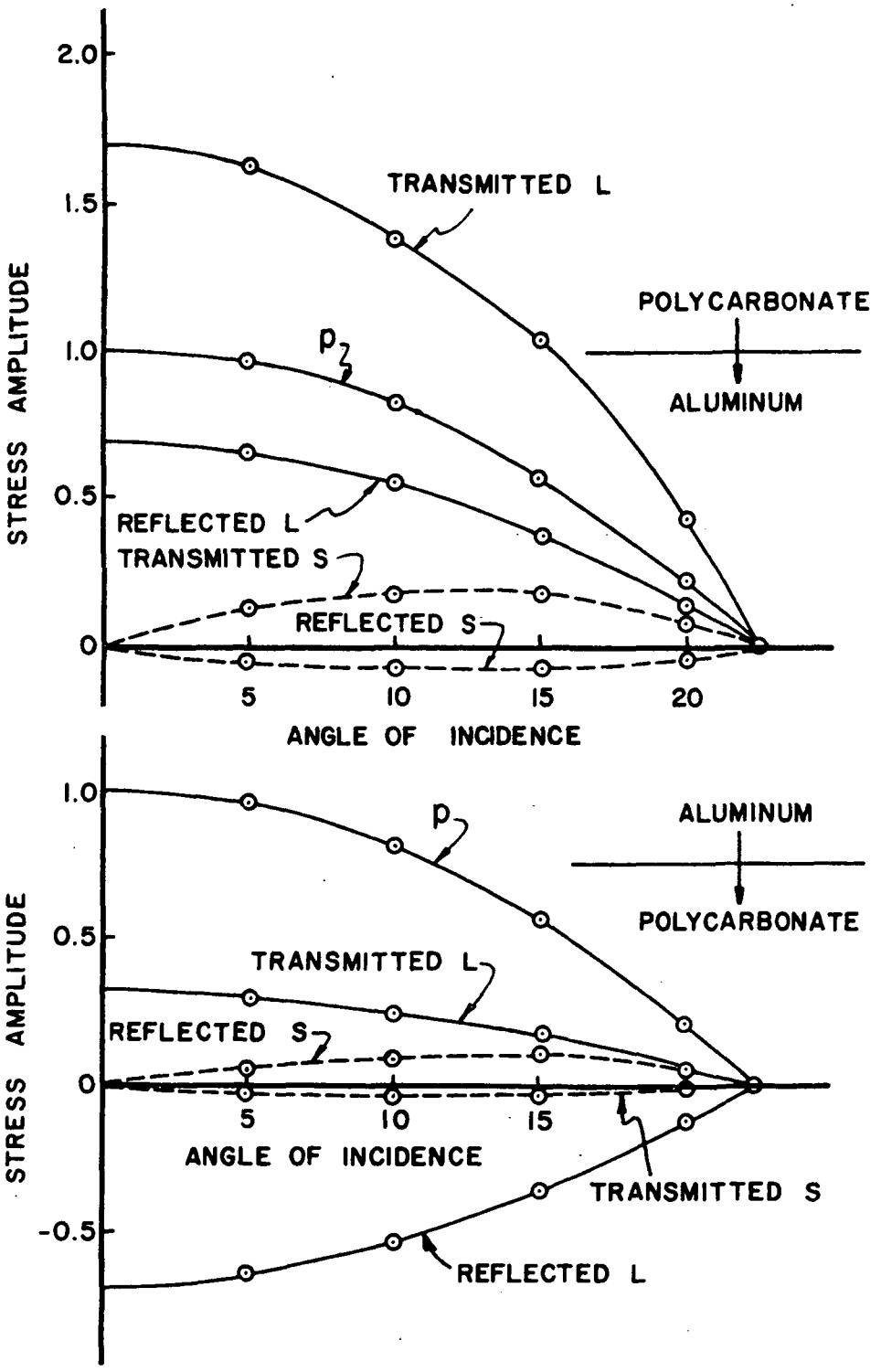

Figure 12. Stress Wave Amplitudes at an Interface
($p = 1 - 6 \tan^2 \theta$)

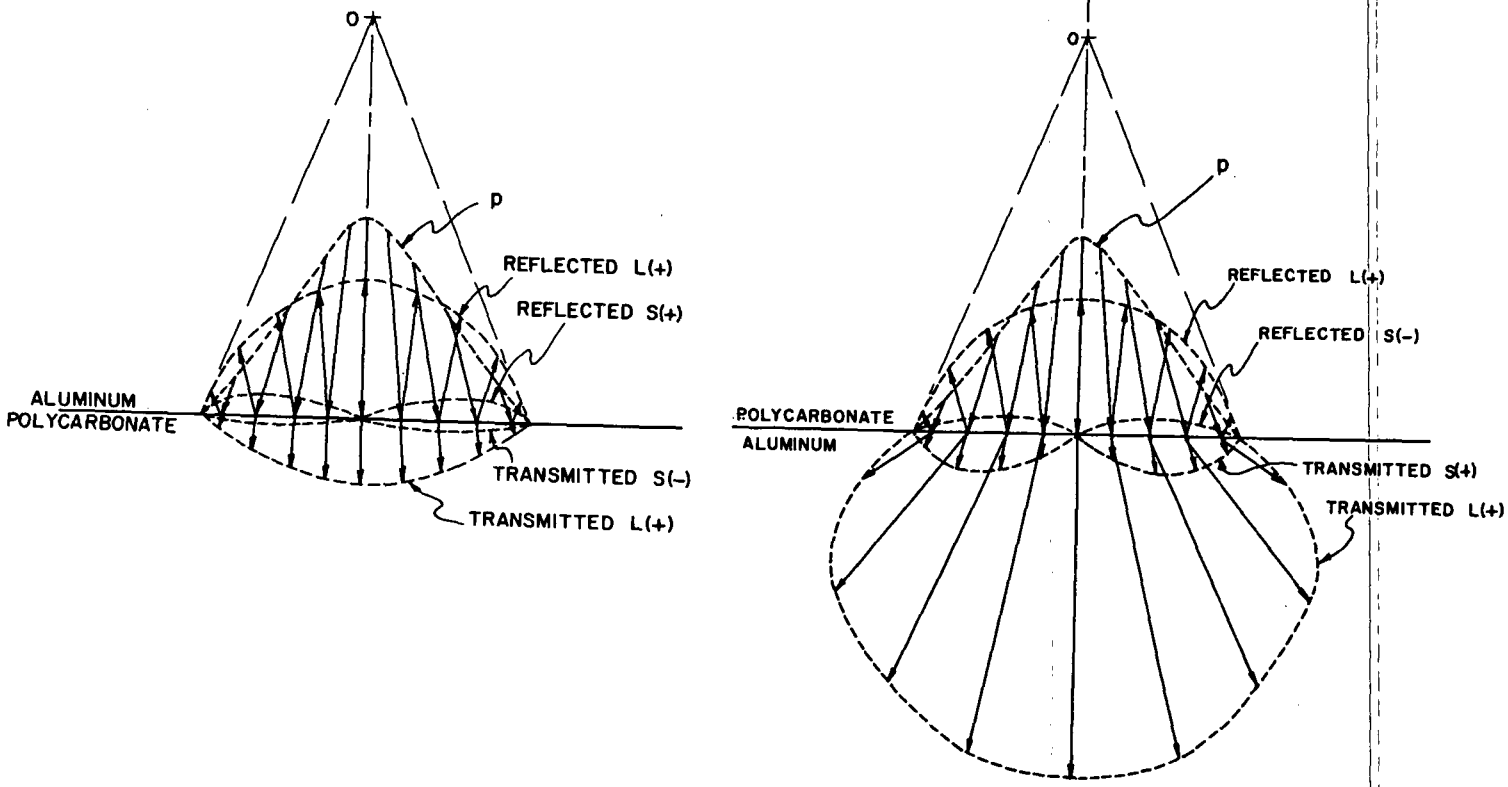

Figure 13. Vector Representation of Transmitted and Reflected Stress Waves ($p = 1 - 6 \tan^2 \theta$)

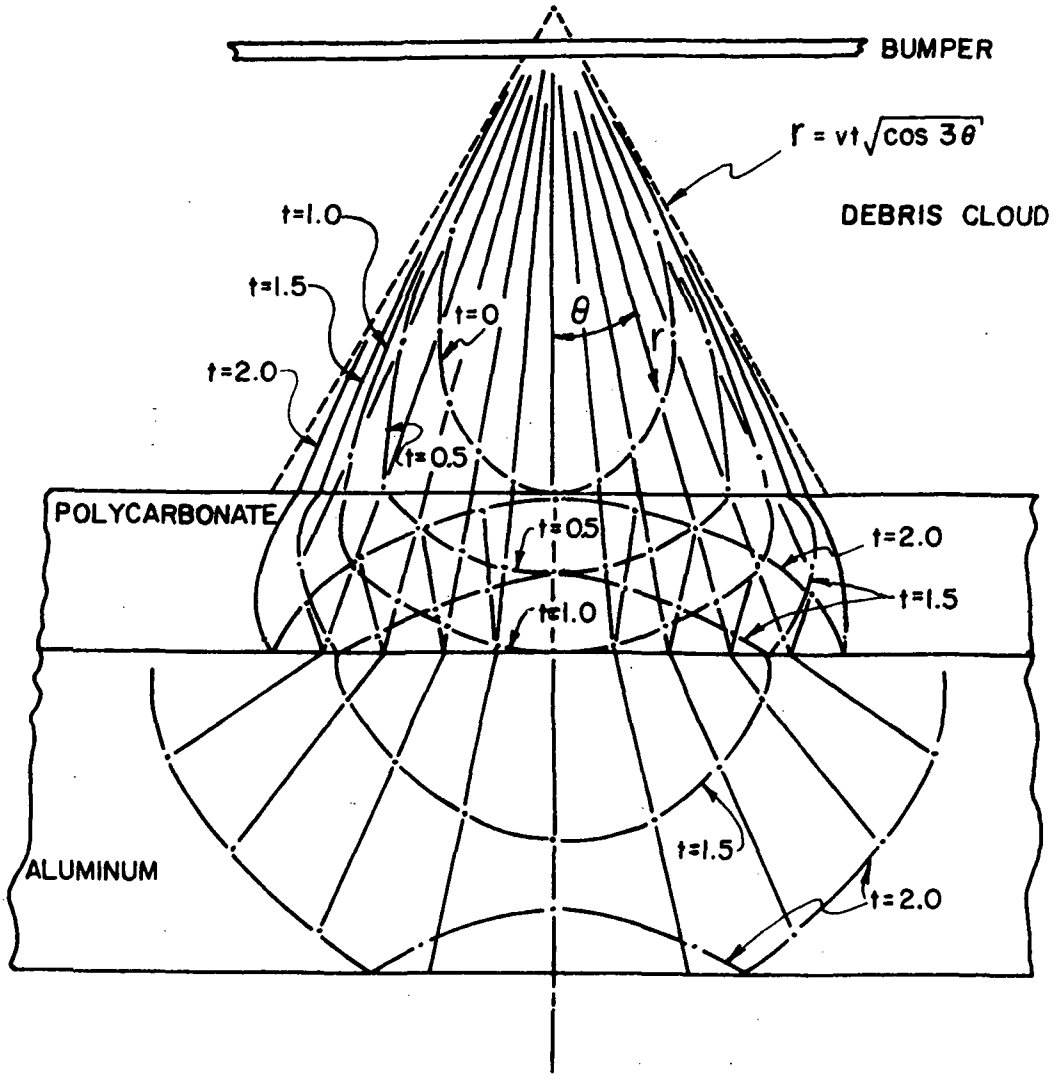

Figure 14. Debris Cloud and Wave Fronts

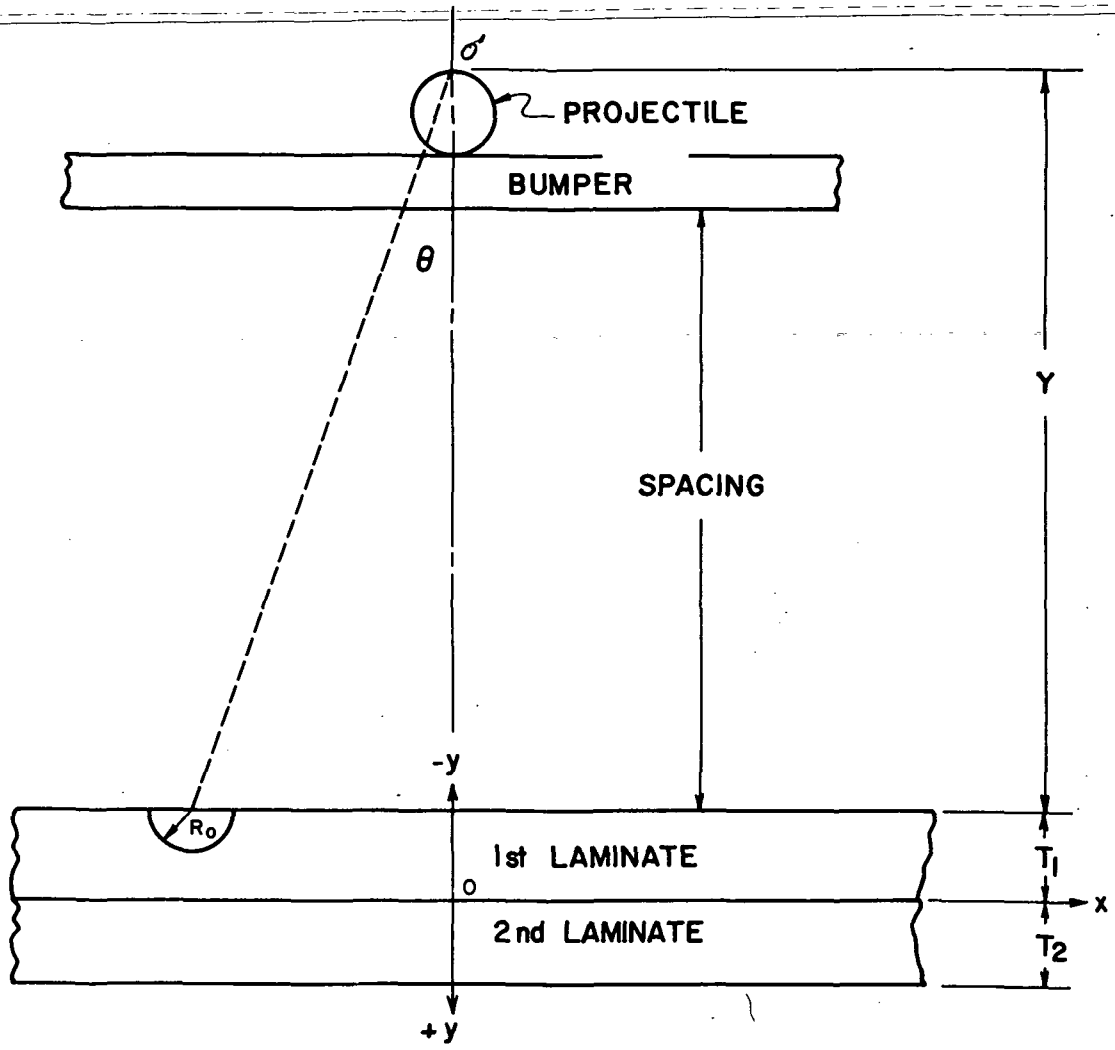

Figure 15. Coordinates and Dimensions

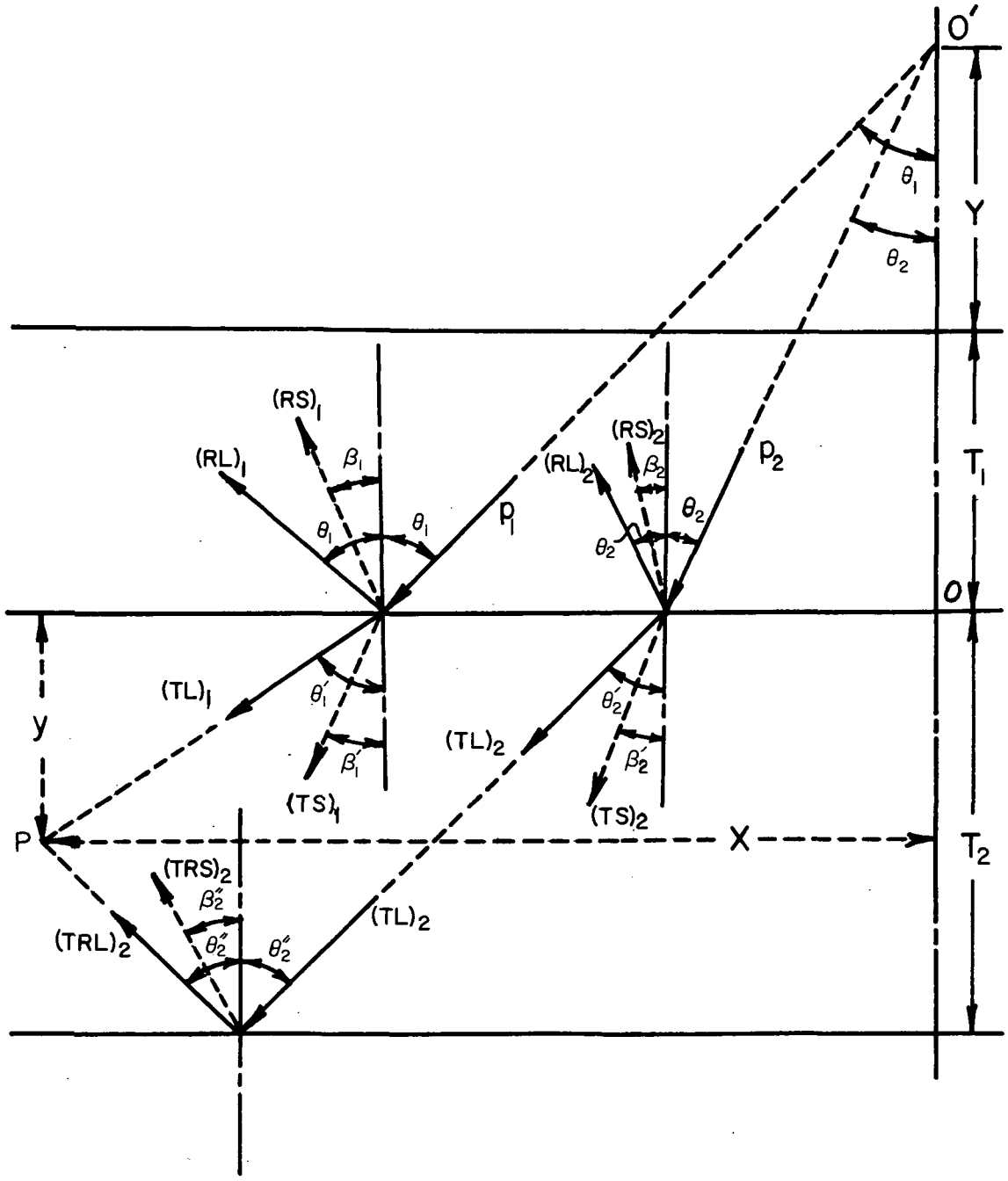

Figure 16. Stress Waves at Interface and Free Surface

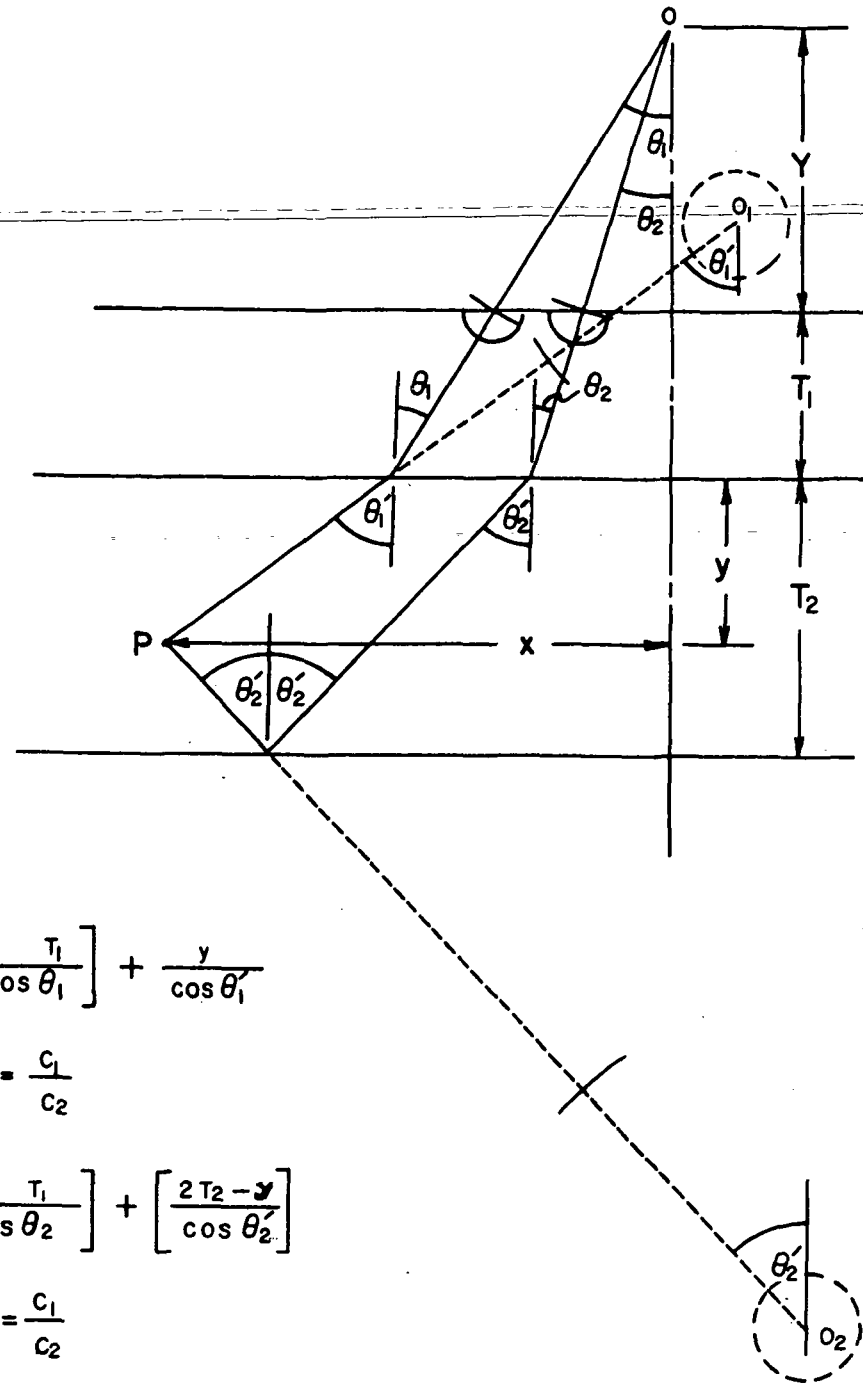

$$R_1 = O_1P = \frac{C_2}{C_1}\left[\frac{T_1}{\cos\theta_1}\right] + \frac{y}{\cos\theta_1'}$$

$$\frac{\sin\theta_1}{\sin\theta_1'} = \frac{C_1}{C_2}$$

$$R_2 = O_2P = \frac{C_2}{C_1}\left[\frac{T_1}{\cos\theta_2}\right] + \left[\frac{2T_2 - y}{\cos\theta_2'}\right]$$

$$\frac{\sin\theta_2}{\sin\theta_2'} = \frac{C_1}{C_2}$$

Figure 17. Locations of Imaginary Cavities

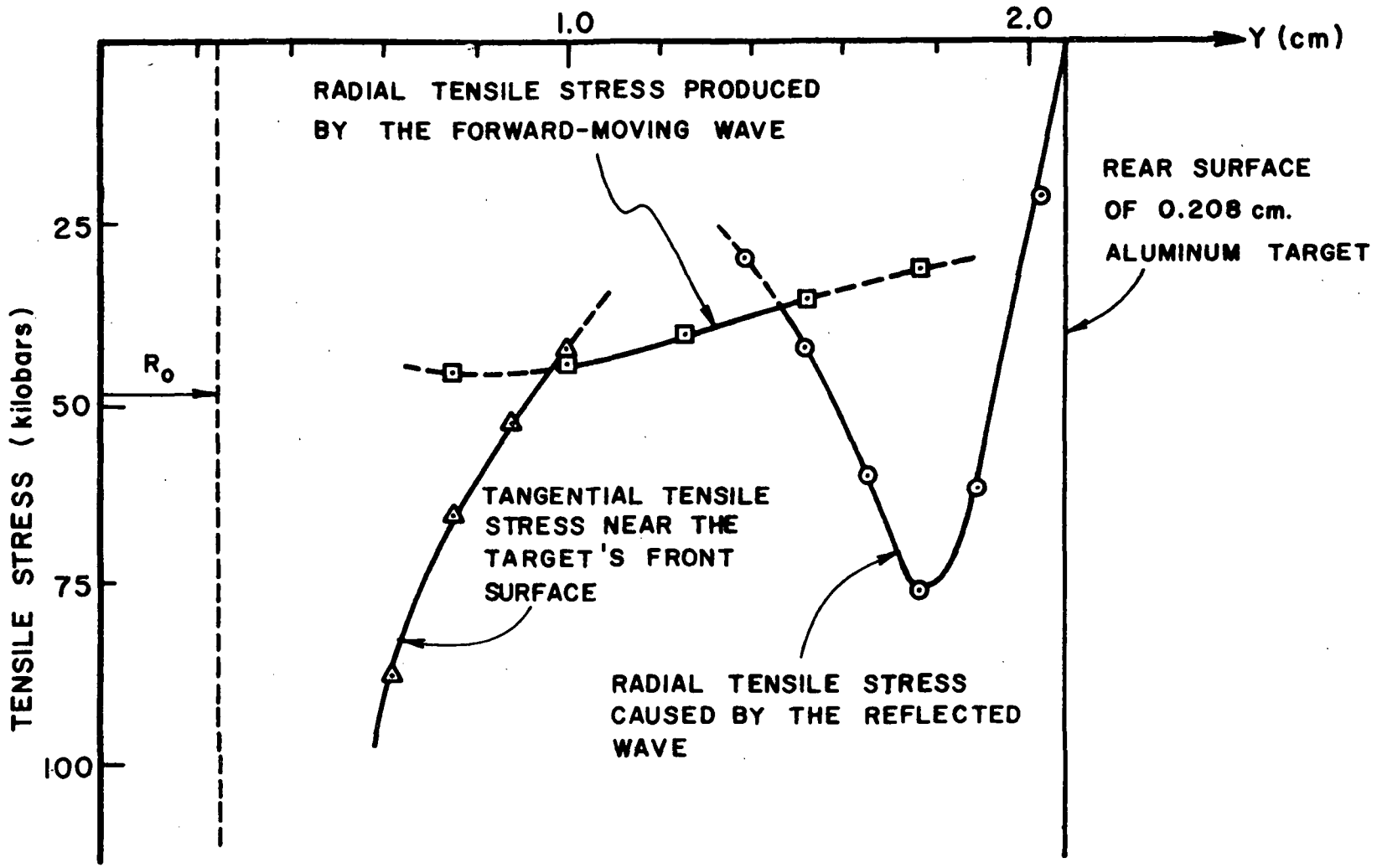

Figure 18. Possible Causes of Tensile Stresses

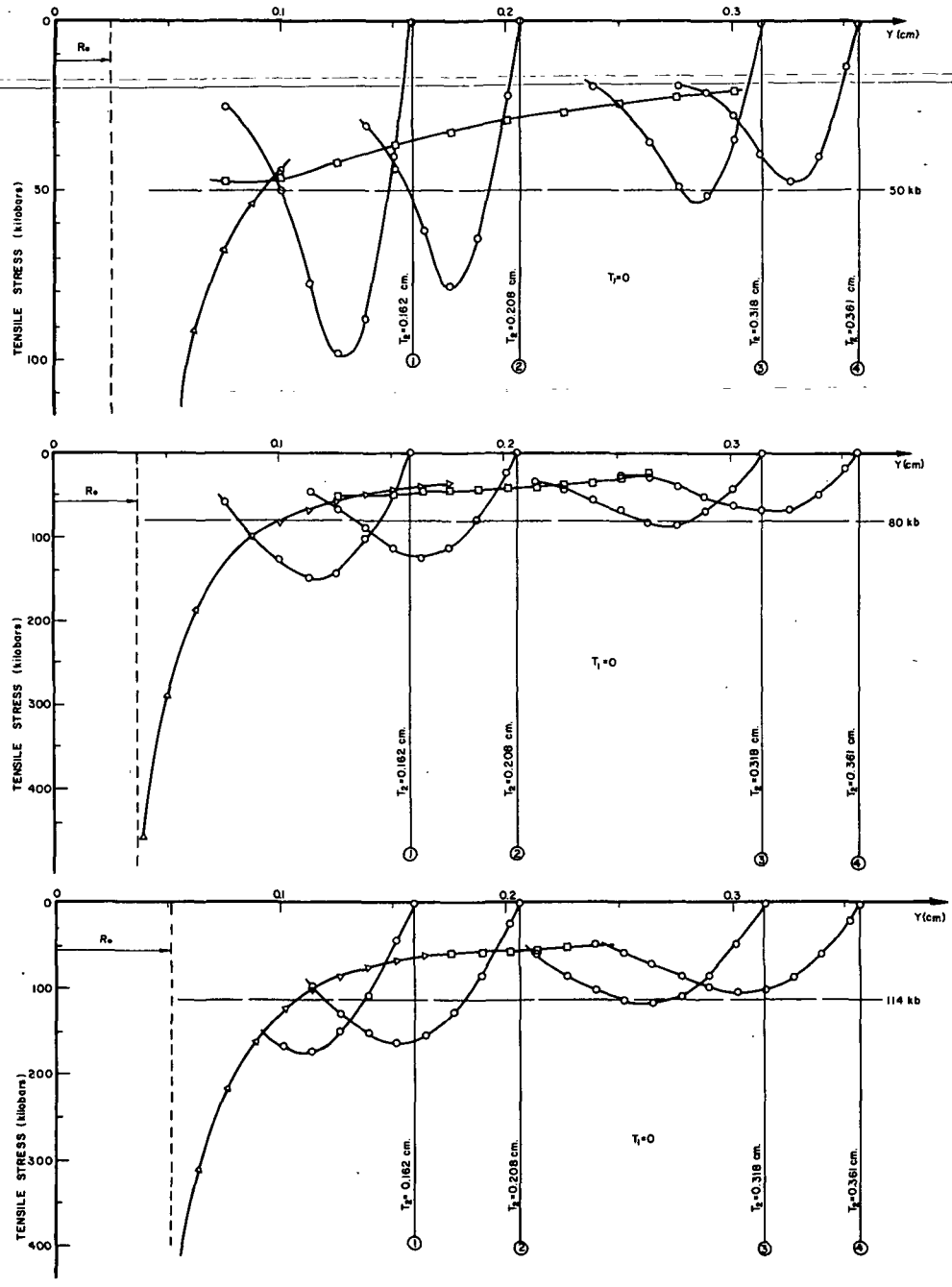

Figure 19. Maximum Tensile Stress Along Y-axis of Solid Aluminum Targets - - Pulse Risetime = 0.05 microsecond

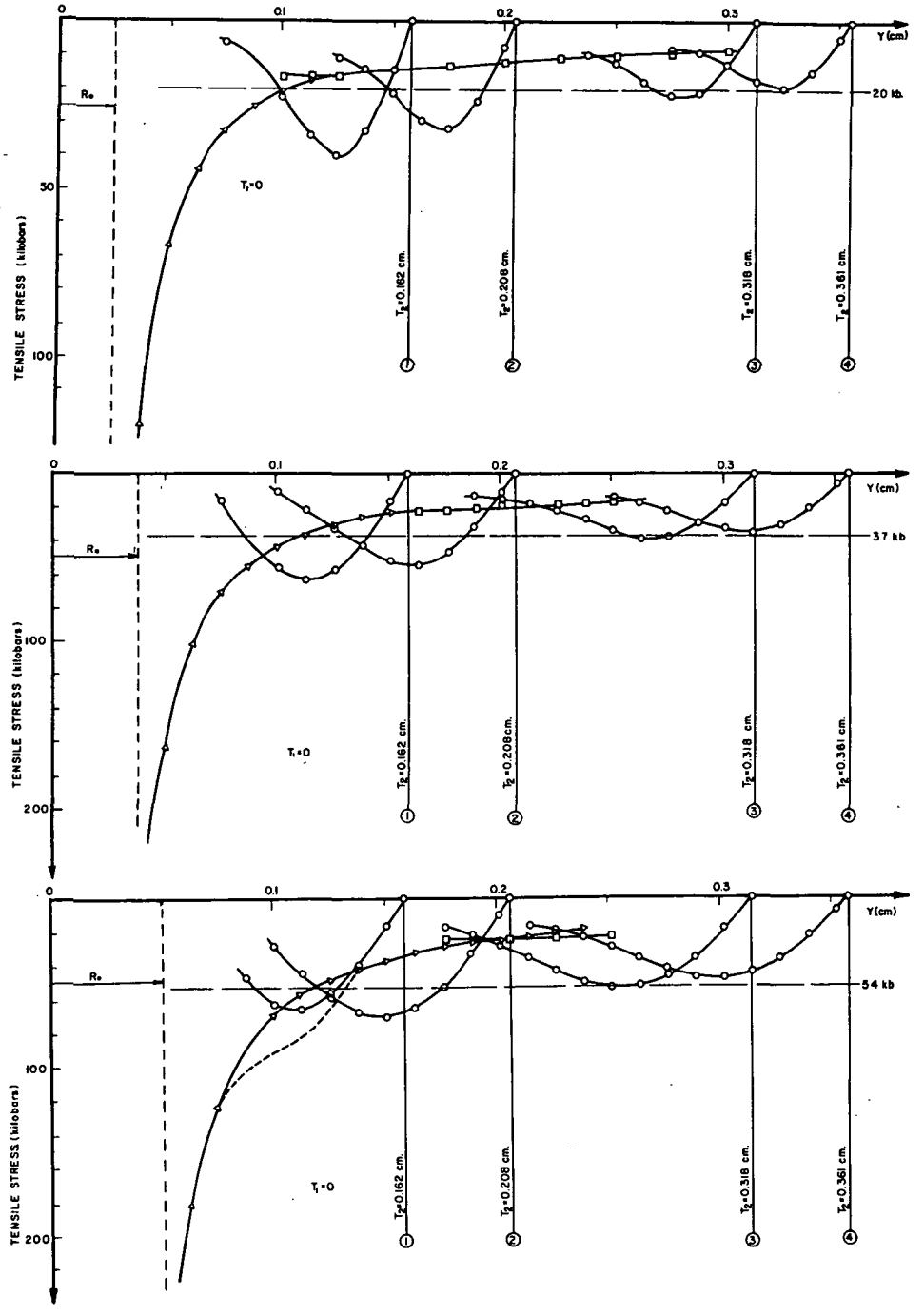

Figure 20. Maximum Tensile Stress Along Y-axis of Solid Aluminum Targets - - Pulse Risetime = 0.10 microsecond

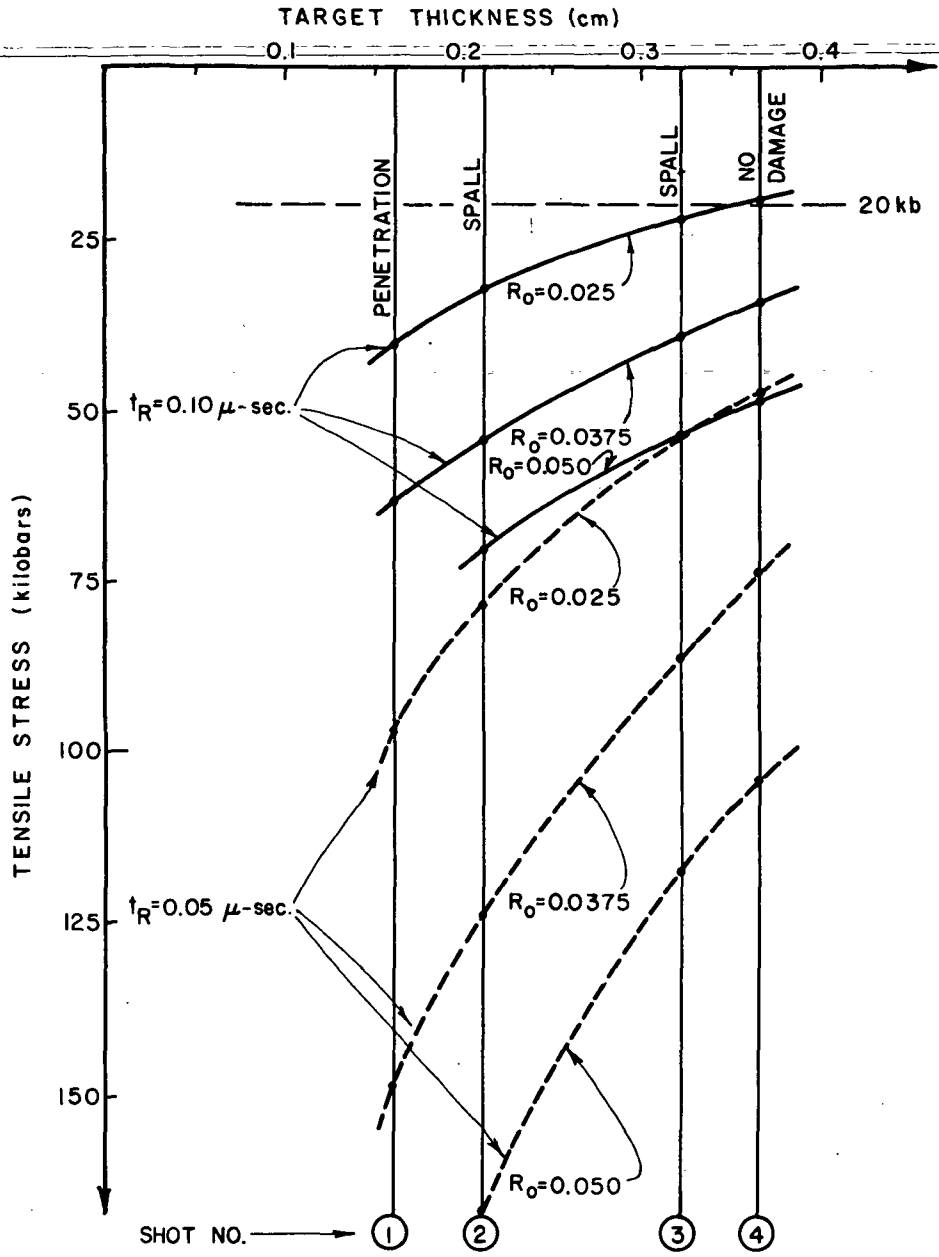

Figure 21. Summary of Analytical and Experimental Results for Solid Aluminum Targets

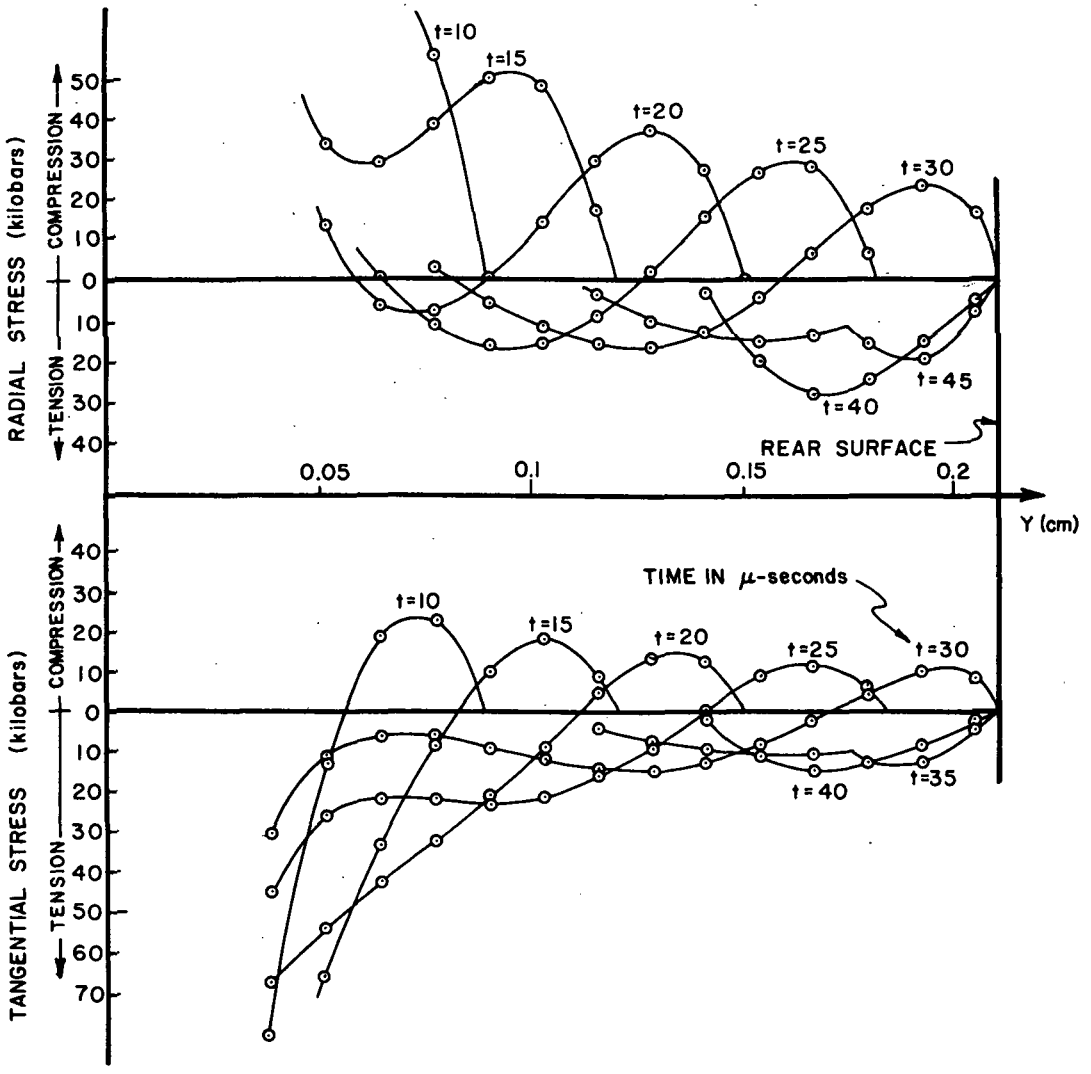

Figure 22. Stress Waves at Various Times

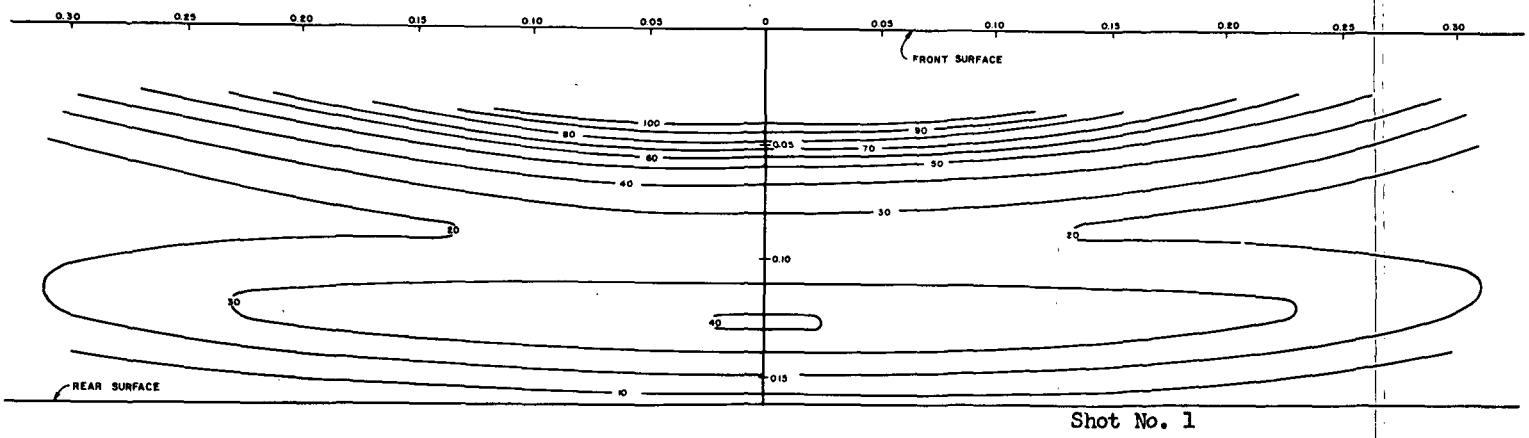

Figure 23. Maximum Tensile Stresses in Solid Aluminum Targets

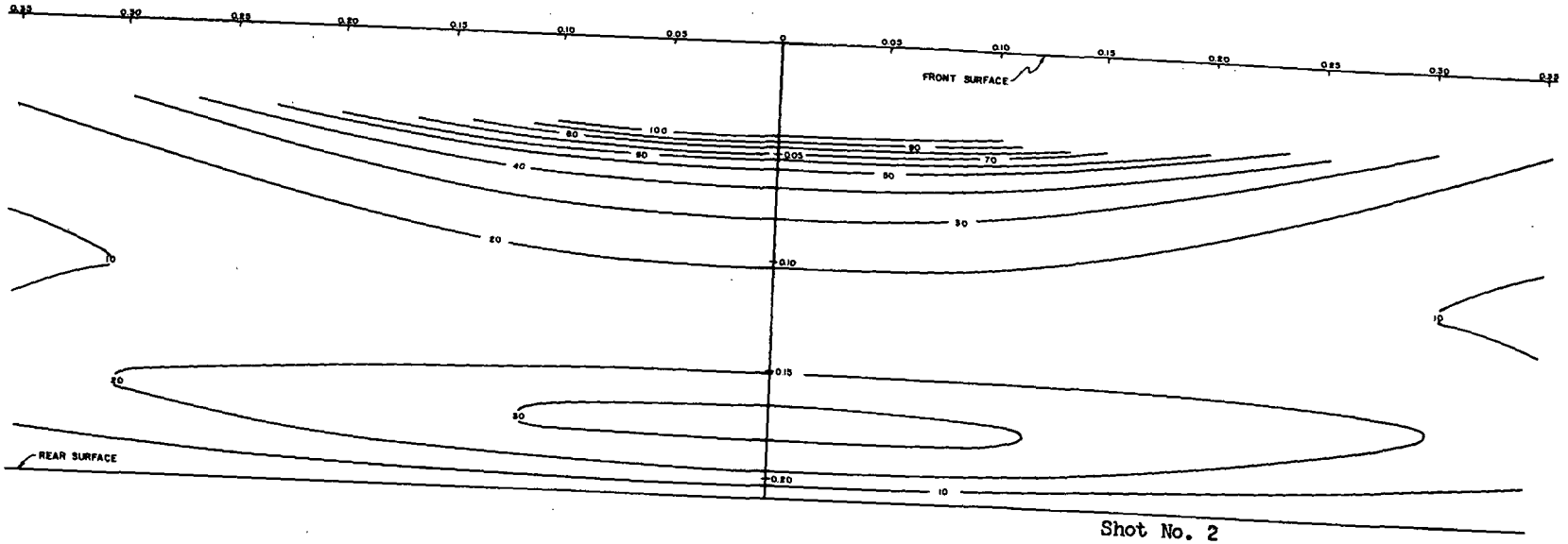

Figure 23. Continued

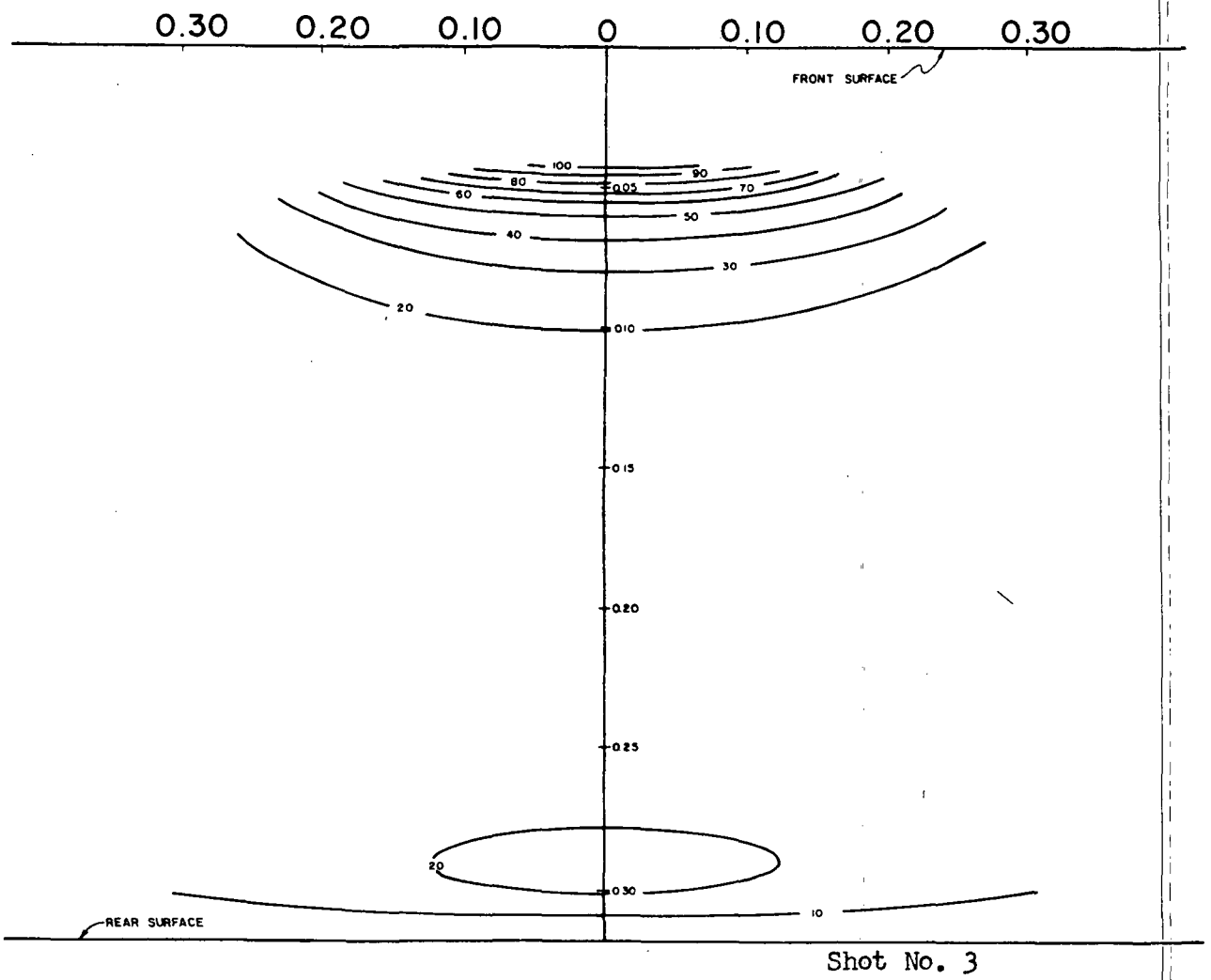

Figure 23. Continued

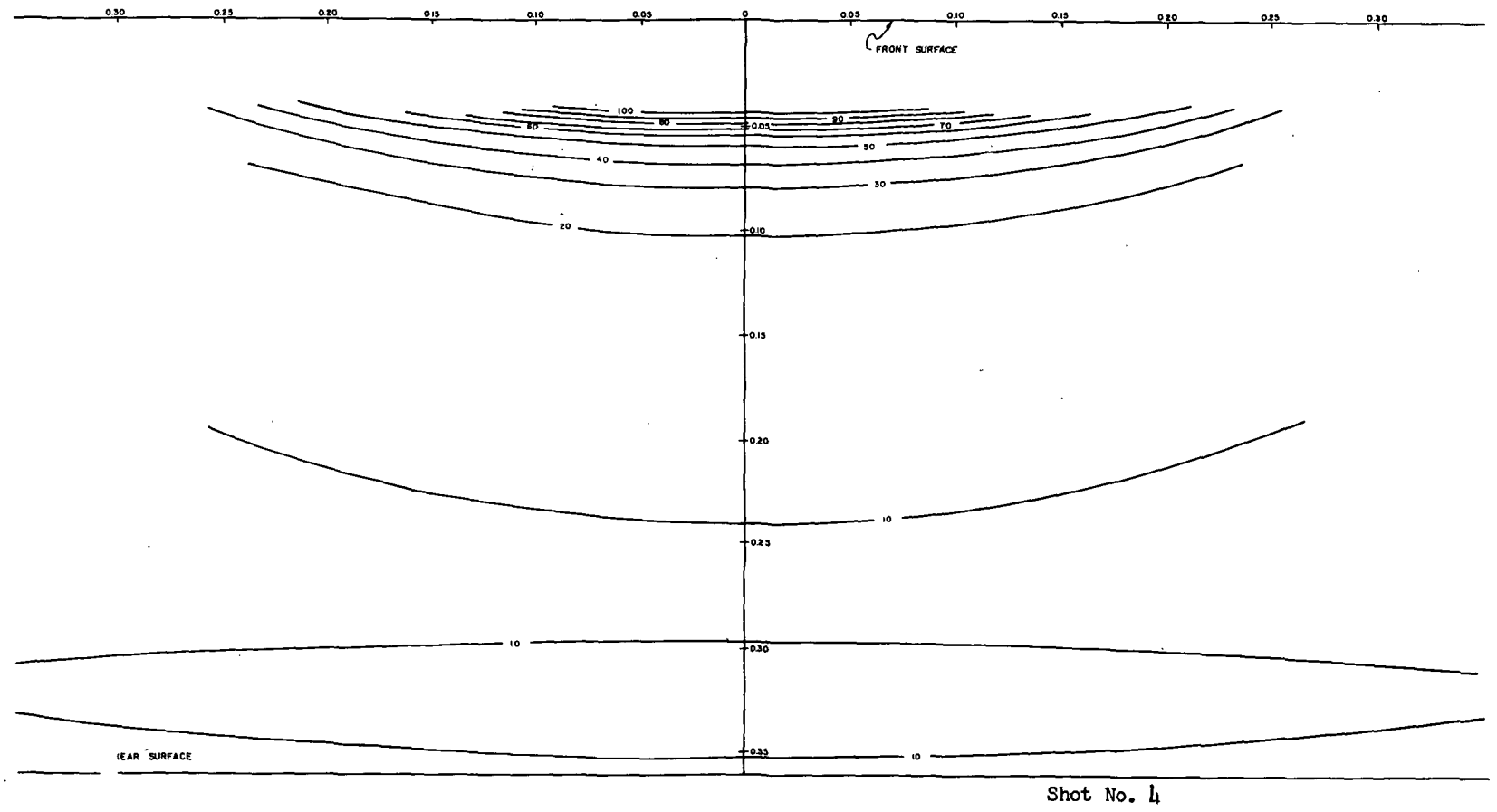

Figure 23. Concluded

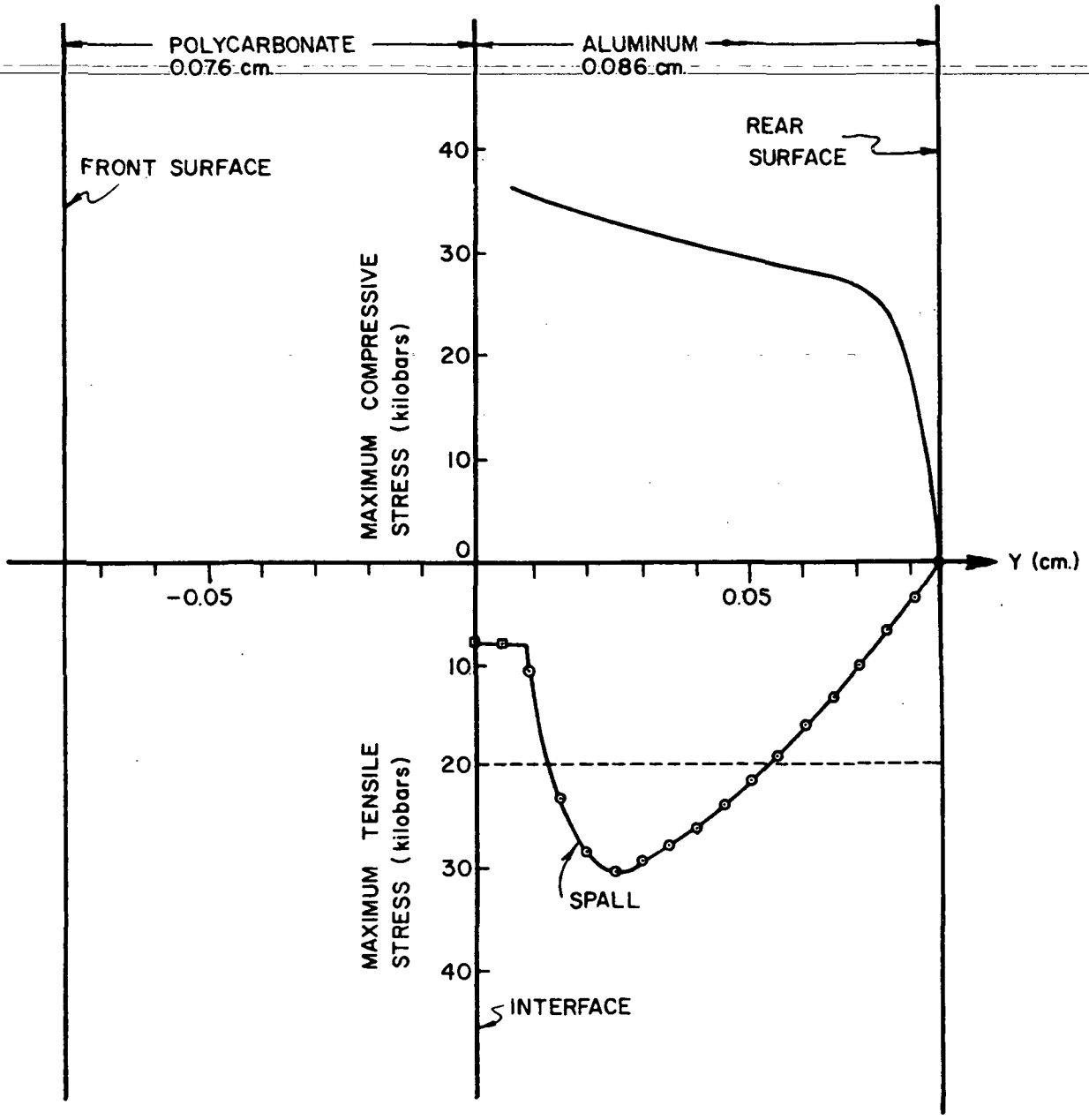

Figure 24. Maximum Stress Along the Y-axis of Laminated Target - Shot No. 5

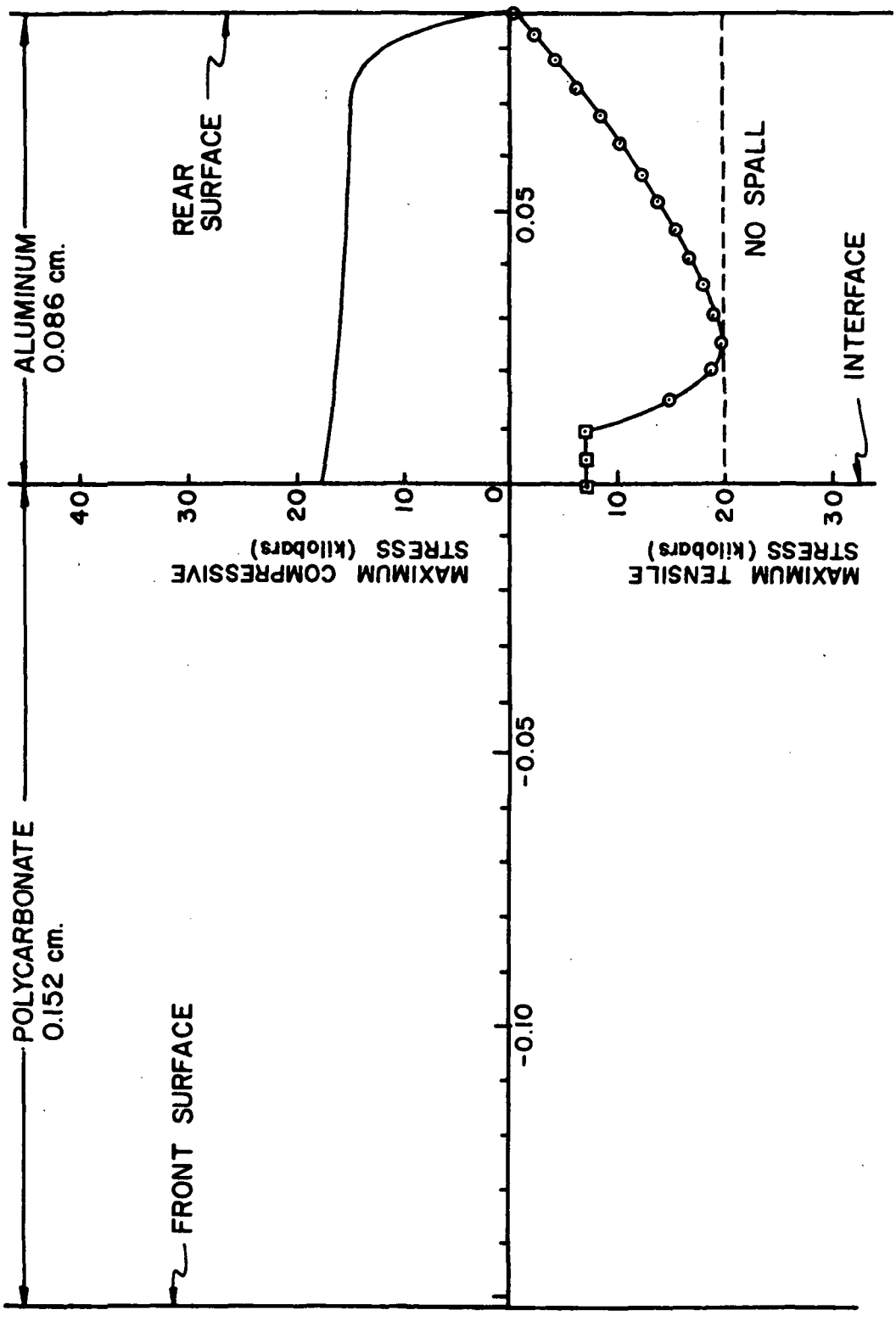

Figure 25. Maximum Stress Along Y-axis of Laminated Target - Shot No. 6

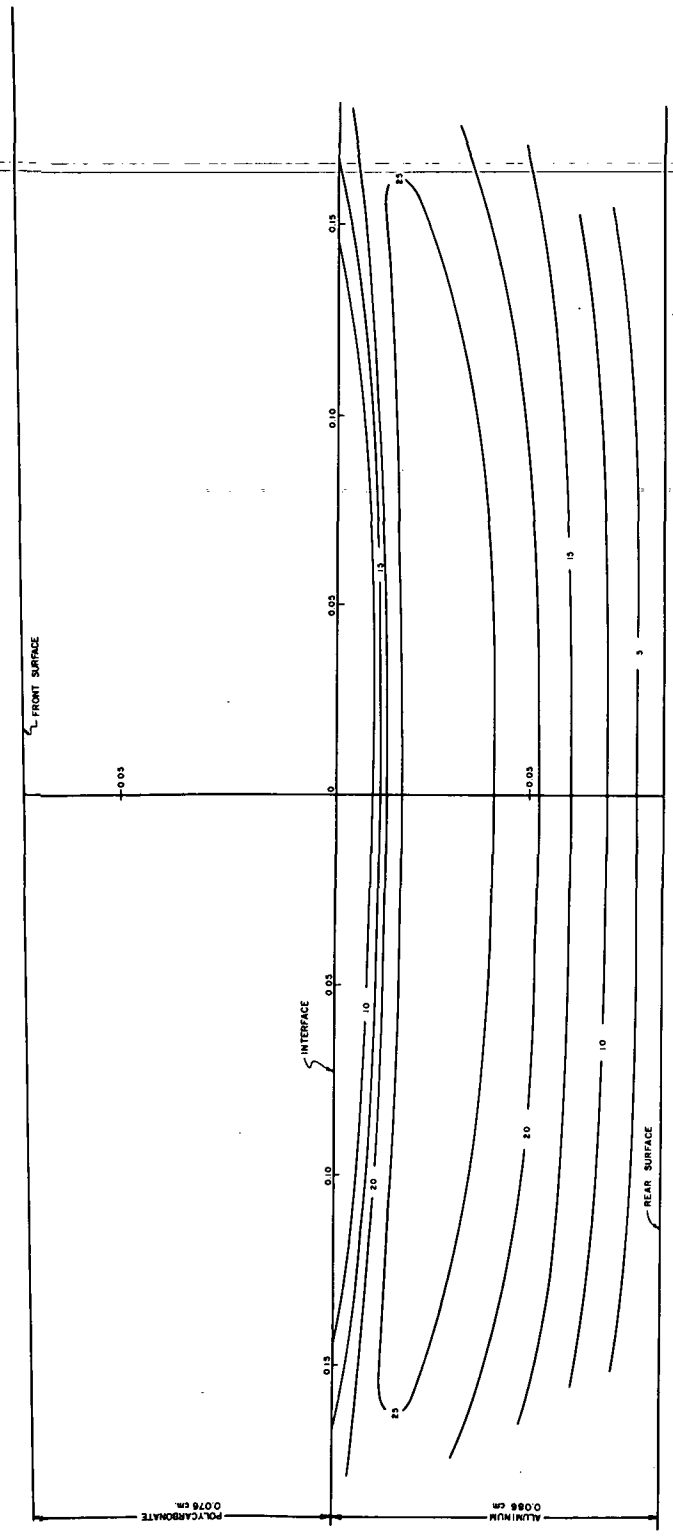

Shot No. 5

Figure 26. Maximum Tensile Stress in Laminated Targets

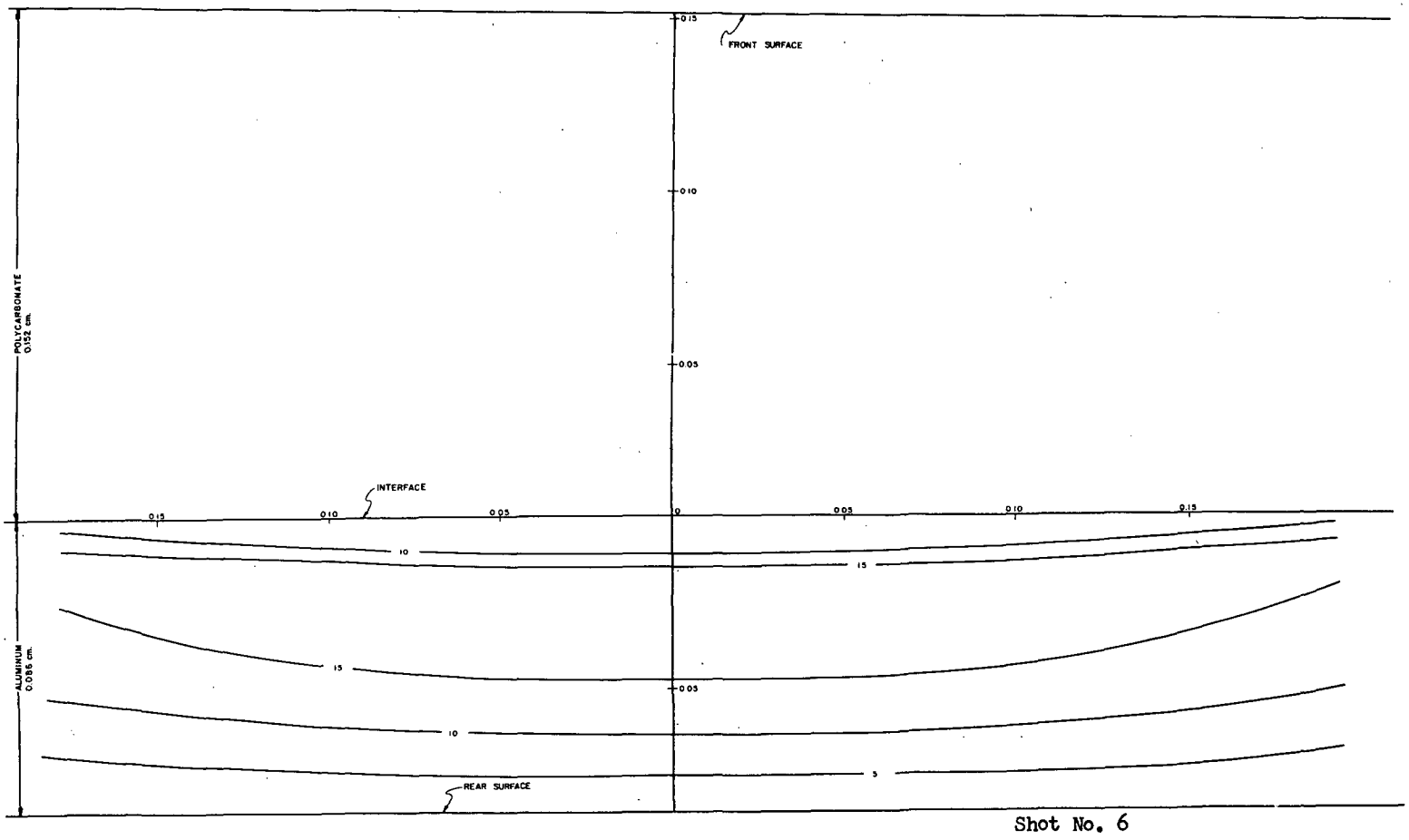

Figure 26. Concluded

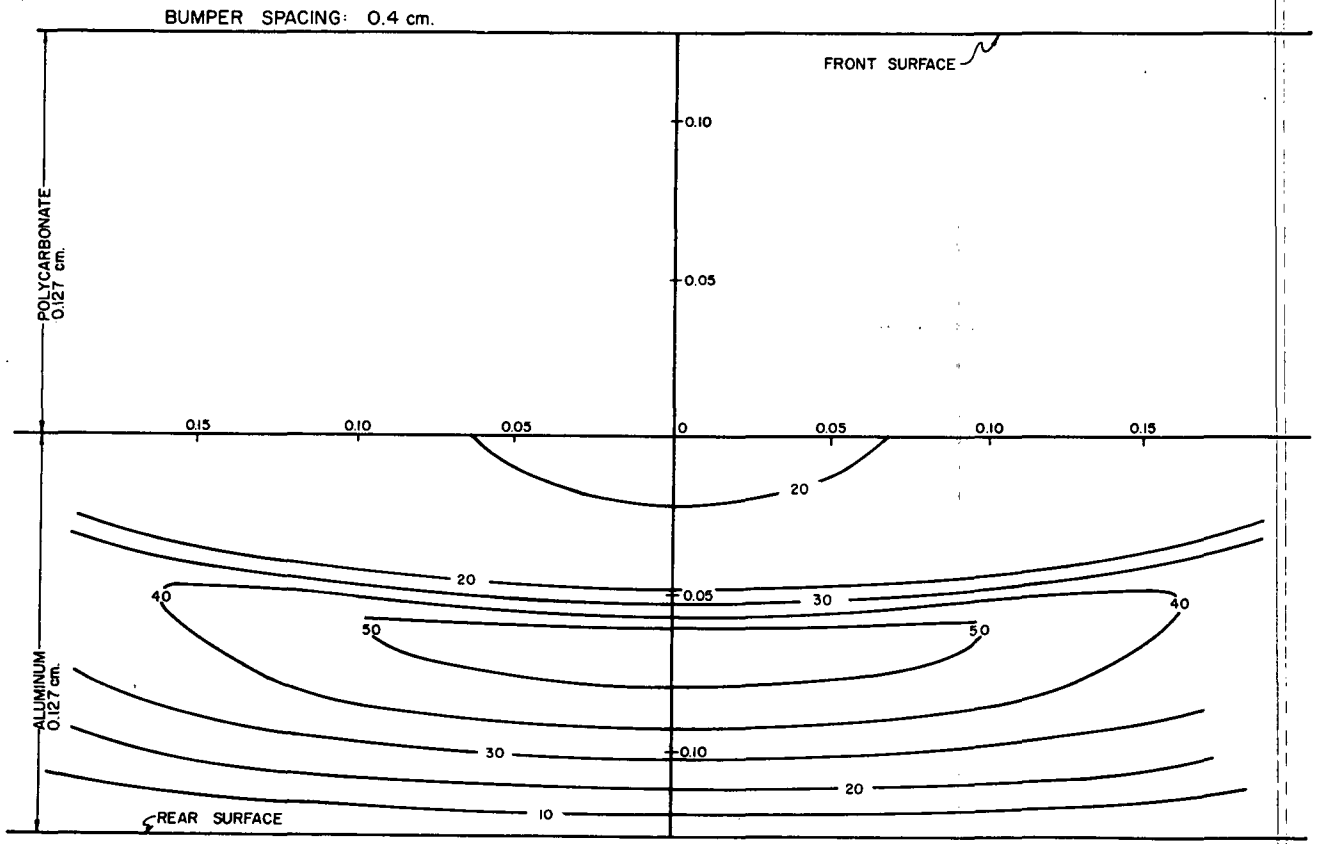

Figure 27. Effect of Bumper Spacing Upon Maximum Tensile Stress

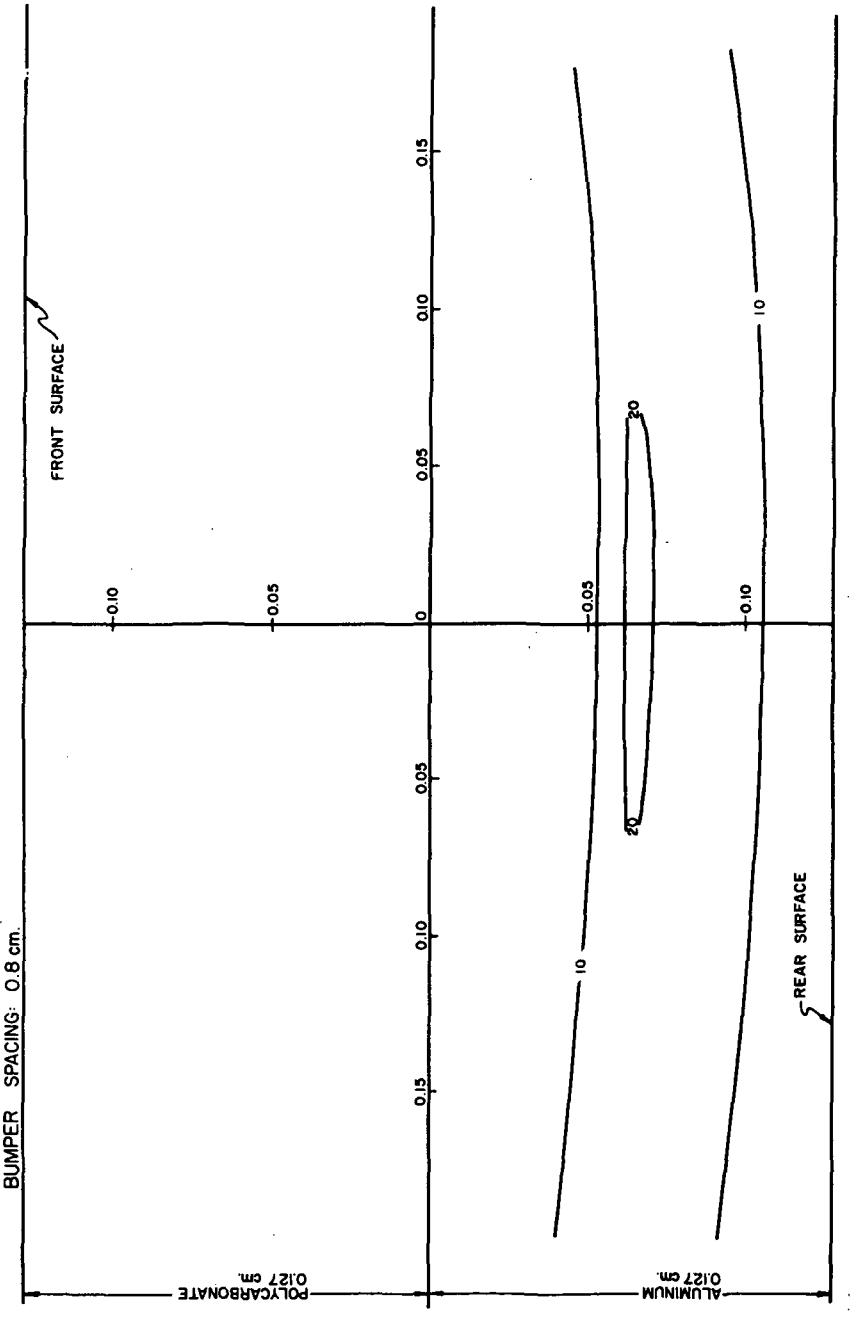

Figure 27. Continued

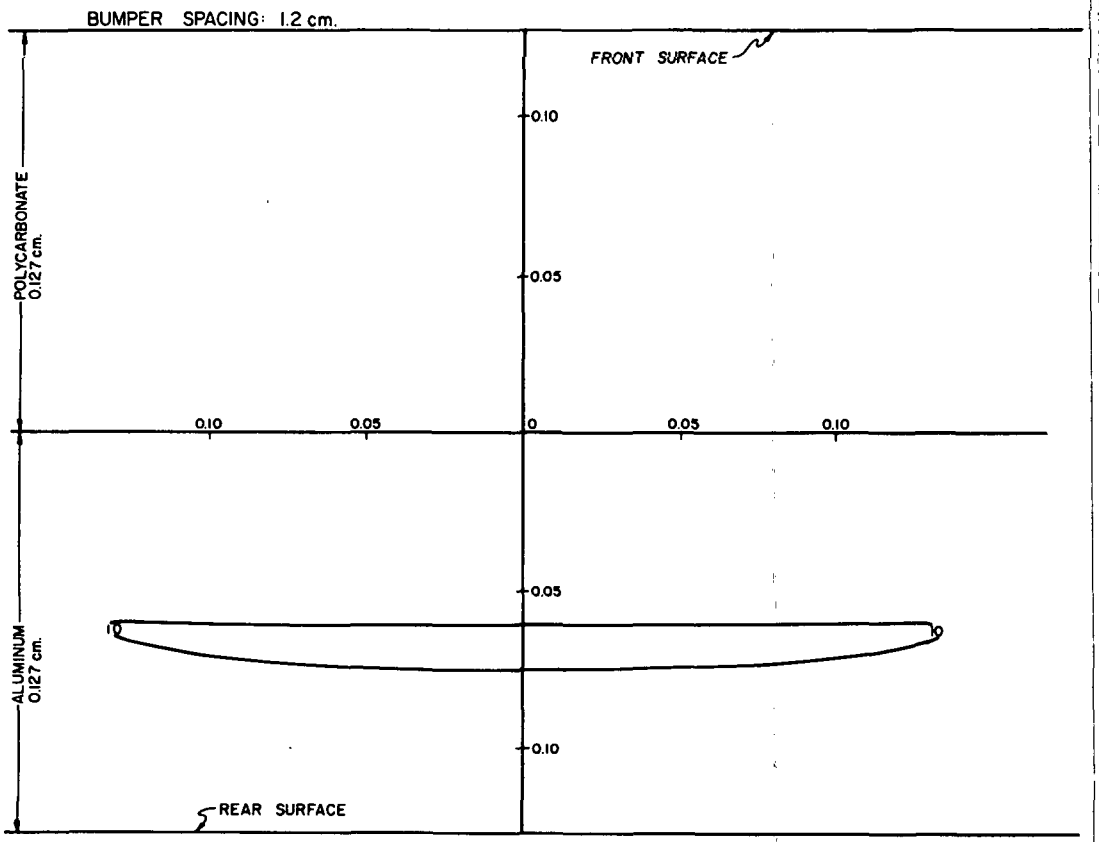

Figure 27. Concluded

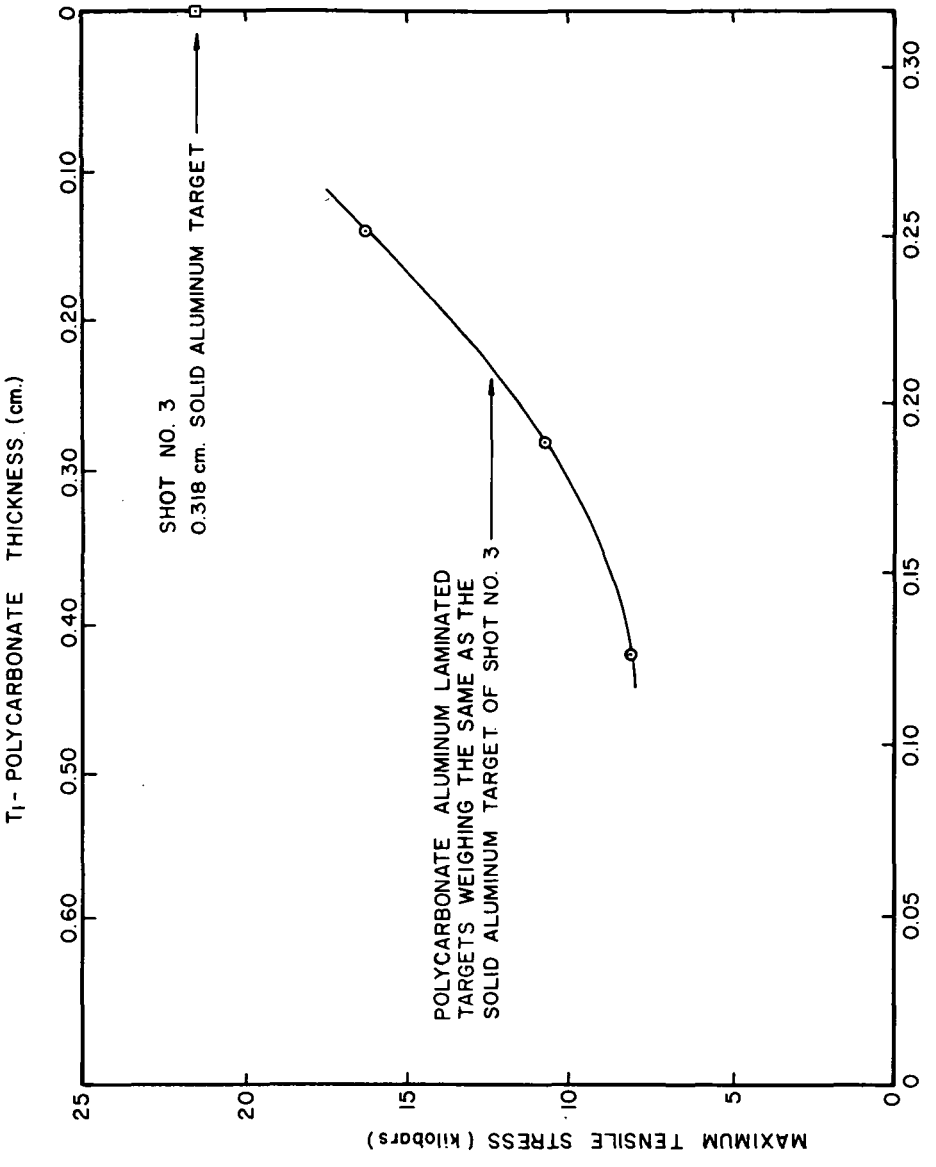

Figure 28. Maximum Tensile Stresses in Laminated Targets of Equal Weight

"The aeronautical and space activities of the United States shall be conducted so as to contribute . . . to the expansion of human knowledge of phenomena in the atmosphere and space. The Administration shall provide for the widest practicable and appropriate dissemination of information concerning its activities and the results thereof."

—NATIONAL AERONAUTICS AND SPACE ACT OF 1958

NASA SCIENTIFIC AND TECHNICAL PUBLICATIONS

TECHNICAL REPORTS: Scientific and technical information considered important, complete, and a lasting contribution to existing knowledge.

TECHNICAL NOTES: Information less broad in scope but nevertheless of importance as a contribution to existing knowledge.

TECHNICAL MEMORANDUMS: Information receiving limited distribution because of preliminary data, security classification, or other reasons. Also includes conference proceedings with either limited or unlimited distribution.

CONTRACTOR REPORTS: Scientific and technical information generated under a NASA contract or grant and considered an important contribution to existing knowledge.

TECHNICAL TRANSLATIONS: Information published in a foreign language considered to merit NASA distribution in English.

SPECIAL PUBLICATIONS: Information derived from or of value to NASA activities. Publications include final reports of major projects, monographs, data compilations, handbooks, sourcebooks, and special bibliographies.

TECHNOLOGY UTILIZATION PUBLICATIONS: Information on technology used by NASA that may be of particular interest in commercial and other non-aerospace applications. Publications include Tech Briefs, Technology Utilization Reports and Technology Surveys.

Details on the availability of these publications may be obtained from:

SCIENTIFIC AND TECHNICAL INFORMATION OFFICE

NATIONAL AERONAUTICS AND SPACE ADMINISTRATION

Washington, D.C. 20546